INFORMATION TO USERS

This manuscript has been reproduced from the microfilm master. UMI films the text directly from the original or copy submitted. Thus, some thesis and dissertation copies are in typewriter face, while others may be from any type of computer printer.

The quality of this reproduction is dependent upon the quality of the copy submitted. Broken or indistinct print, colored or poor quality illustrations and photographs, print bleedthrough, substandard margins, and improper alignment can adversely affect reproduction.

In the unlikely event that the author did not send UMI a complete manuscript and there are missing pages, these will be noted. Also, if unauthorized copyright material had to be removed, a note will indicate the deletion.

Oversize materials (e.g., maps, drawings, charts) are reproduced by sectioning the original, beginning at the upper left-hand corner and continuing from left to right in equal sections with small overlaps. Each original is also photographed in one exposure and is included in reduced form at the back of the book.

Photographs included in the original manuscript have been reproduced xerographically in this copy. Higher quality 6" x 9" black and white photographic prints are available for any photographs or illustrations appearing in this copy for an additional charge. Contact UMI directly to order.

UMI

A Bell & Howell Information Company
300 North Zeeb Road, Ann Arbor MI 48106-1346 USA
313/761-4700 800/521-0600

Downloaded from SHAREOK. Persistent Handle URL: https://hdl.handle.net/11244/5445

UNIVERSITY OF OKLAHOMA

GRADUATE COLLEGE

ADVANCED COMPUTATIONAL METHODS IN ACOUSTIC TOMOGRAPHY

A Dissertation

SUBMITTED TO THE GRADUATE FACULTY

in partial fulfillment of the requirements for the

degree of

Doctor of Philosophy

By

CLAIRE SULLIVAN

Norman, Oklahoma

1997

UMI Number: 9722334

UMI Microform 9722334
Copyright 1997, by UMI Company. All rights reserved.

This microform edition is protected against unauthorized
copying under Title 17, United States Code.

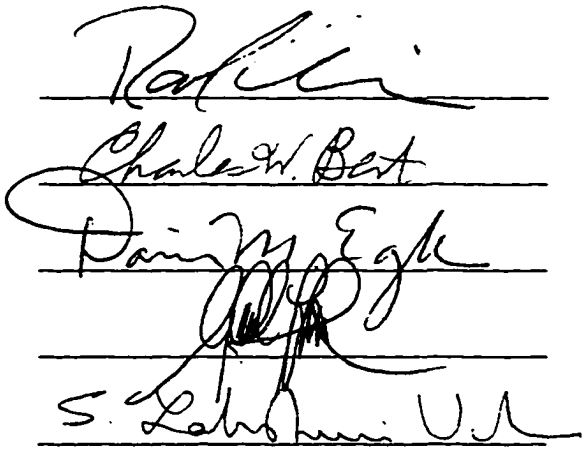
UMI
300 North Zeeb Road
Ann Arbor, MI 48103

ADVANCED COMPUTATIONAL METHODS IN ACOUSTIC TOMOGRAPHY

A Dissertation

APPROVED FOR THE SCHOOL OF AEROSPACE

AND MECHANICAL ENGINEERING



© Copyright by CLAIRE SULLIVAN 1997

All Rights Reserved

ACKNOWLEDGEMENTS

I would like to acknowledge the support and encouragement of my major advisor, Dr. R. Kline. The members of my committee, Dr. A. Striz, Dr. C. Burt, Dr. D. Egle and Dr. S. Lakshmivarahan provided valuable proofreading and discussion. I am extremely grateful to my husband, Chuck Gaw, for his eternal patience and endless confidence.

TABLE OF CONTENTS

LIST OF FIGURES vi

LIST OF TABLES viii

ABSTRACT ix

Chapter

I. INTRODUCTION 1

II. THEORETICAL BACKGROUND 8

III. PARALLEL PROCESSING 26

IV. RAY-BASED TOMOGRAPHIC RECONSTRUCTIONS 34

V. FULL-FIELD TOMOGRAPHIC RECONSTRUCTIONS 59

VI. CONCLUSIONS 82

REFERENCES 85

LIST OF FIGURES

Figure 2.1 Geometry of a laminate 21

Figure 3.1 Matrix addition of two arrays 29

Figure 4.1 Illustration of model discretization 36

Figure 4.2 Ray paths in heterogeneous media 40

Figure 4.3 Illustration of geometric ray tracer 41

Figure 4.4 Pixel grid with stored velocity information 44

Figure 4.5 Time delay curves 47

Figure 4.6 Models used in velocity reconstructions 49

Figure 4.7 Source-receiver geometries 51

Figure 4.8 Epstein layer velocity reconstructions 51

Figure 4.9 Tomographic reconstructions of two-layer model 53

Figure 4.10 Comparison of convergence rates for different models..... 54

Figure 4.11 Convergence rates for different polynomial time delay curves 55

Figure 4.12 Cross-sectional snapshots of convergence process 56

Figure 4.13 Comparison of CPU time 57

Figure5.1 Source and receiver locations 66

Figure5.2 Effect of small angle change on time delay 29

Figure5.3 Convergence of tomographic reconstruction 36

Figure 5.4 Tomographic reconstructions of a ten-degree rotation ,..... 40

Figure 5.5 Location of cross-section 73

Figure 5.6 Snapshot of convergence process 74

Figure 5.7 Tomographic reconstructions of a two-degree rotation 76

Figure 5.8 Effect of perturbation angle on reconstruction results 77

Figure 5.9 Tomographic reconstruction of a +/- five-degree rotation 79

Figure 5.10 Tomographic reconstruction of a +/- five-degree rotation 80

Figure 5.11 Reconstruction with a second-order approximation to the derivative .81

LIST OF TABLES

Table 2.1 Material properties for a glass/epoxy composite..... 24

ABSTRACT

In this work, two methods of acoustic tomography are introduced. Advanced computational methods are implemented to handle the complexity of the tomographic algorithm in isotropic and anisotropic materials. Parallel processing is a technique used to improve the performance and thus the versatility of the method. The speed-up using parallel processing techniques is presented.

A matrix domain decomposition of the ray tracer and the tomography algorithm is presented. This technique is applied to a heterogeneous isotropic material and the velocity is reconstructed. Each processor is assigned a grid point in the discretized model, allowing all source-receiver pair calculations to be performed simultaneously. The CPU time remains relatively constant as the array size increases.

An alternative approach is based on the field theory of wave propagation. A finite difference solution of the wave equation for an anisotropic medium is used. The material properties can be reconstructed using a modification of the traditional ART (algebraic reconstruction technique). The rotation angle of a fiber-reinforced laminate is reconstructed in this study. The algorithm is successful in detecting two, five and ten-degree misalignments in an orthotropic composite laminate.

CHAPTER I

INTRODUCTION

Composite materials are complex structures widely utilized in modern industry. Numerous nondestructive testing techniques are used to examine these composites for manufacturing flaws, including ultrasonic and x-ray testing. Tomographic image reconstructions, while commonly used for x-ray data, are less often used to analyze acoustic data. In general, tomograms provide an excellent means of obtaining local velocity information about a non-homogenous medium. In turn, the velocity field provides information about numerous parameters such as the stiffness, degree of matrix cure, and lay-up parameters of the composite. However, unlike x-rays, acoustic rays do not travel in a straight line through heterogeneous material. This increases the computational requirements of this technique. In addition, the anisotropic nature of composites complicates ultrasonic testing due to the directional dependence of the velocity. Increased utilization of acoustic tomography for practical applications requires increasing the speed and accuracy of the reconstruction algorithm. The present work develops a parallel processing approach to achieve this goal.

Two different computational techniques were used to create the tomographic reconstructions. The first used a ray-tracing technique to track the progression of the wave front through the material. The ray-tracing procedure and the inversion algorithm are computed in parallel, significantly reducing the computation time. The models tested were constructed of isotropic materials with layers of varying velocities. The tomograms reconstructed these velocities. The second technique used a finite-difference solution to the wave equation to calculate the progression of the wavefront through the material. This approach directly accounts for material anisotropy and ray bending. The technique was used to construct the local variations in fiber reinforcement angles in orthotropic composite laminates.

The following sections introduce a history of tomography and parallel processing, and a review of recent work in the field. A theoretical background of wave propagation in anisotropic materials and the micromechanics of composite materials are presented. This is followed by a discussion of parallel processing techniques. Then, the algorithm designs and the accompanying results are presented.

1.1 Tomography

The Greek derivation of tomography means, "picture of a slice". X-ray tomography is defined as " a diagnostic technique using x-ray photographs in which the shadows of structures before and behind the section under scrutiny do not show"[1]. X-ray tomography is employed in medicine and nondestructive evaluation of materials

(NDE). However, other forms of energy, such as microwaves in the field of astronomy, may also be used to reconstruct an image. Acoustic tomography utilizes sound waves propagating through the medium to build an image. This technique is used in the fields of medicine, seismology and NDE. Acoustic tomography is safer and less expensive then x-ray tomography, and it penetrates deeper into the material than any other form of energy. X-rays are sensitive only to density contrasts, but acoustic waves can be used to measure both velocity and attenuation changes through the material. The main disadvantage of acoustic tomography is that an acoustic wave does not travel in a straight line through a heterogeneous material. Therefore the ray paths are additional unknowns when trying to reconstruct an image. Further complications are present with anisotropic materials since the velocity is dependent on the direction of the acoustic rays passing through the material.

Johann Radon discovered the fundamental mathematical tool for tomography in 1917. He proved that any two-dimensional object could be uniquely reconstructed from an infinite set of projections[2]. The reconstructed functions were developed from line integral data using the Radon transformation. Other mathematicians, radio astronomers, and workers in optics and medical radiology independently rediscovered this work[2].

The first practical application of Radon's work was in 1956, nearly forty years later. A radio astronomer, Bracewell, used the Radon transform to map regions of microwave radiation from the sun[2]. Medical applications of x-ray tomography were first introduced in 1963, but did not become widespread until the early 1970's, after

the development of Hounsfield's CT scanning equipment[3]. The application of ultrasonic energy to computed tomography was first proposed by Greenleaf in the mid 1970's.[4]

1.2 Literature Review

Interest in acoustic tomography has increased significantly, especially in the geophysical arena. This is due mainly to the application of pre-stack depth migration to 3-D seismic data, which has contributed to two recent major hydrocarbon discoveries in the Gulf of Mexico[5]. Pre-stack depth migration of seismic data allows the acoustic imaging of sedimentary strata below the large salt structures present there[5]. The development of an accurate velocity model for the salt and the surrounding sediments is a key step in pre-stack depth migration. Advances in computer technology have been essential in the commercial development of this technique[6].

The most computationally intensive part of acoustic tomography techniques based on ray theory is the tracing of the acoustic ray paths through heterogeneous media. Most of the current work in acoustic tomography has been directed at improving the ray tracing algorithm or eliminating the need for ray tracing altogether. Traditional ray tracing approaches are based on Snell's law (Lytle and Dines[7]) and on Fermat's principle of minimum time (Um and Thurber[8]). Improvements in the ray tracing algorithms have concentrated on increasing speed and accuracy. Asakawa and Kawanaka[9] used linear travel time interpolation, Zhu and Chun[10] used asymptotic ray

theory and perturbation techniques. Fischer and Lees[11] and Moser[12] refined shortest path ray tracing (SPR) with sparse graphs. Perturbation methods have been advanced by Snieder and Sambridge[13] and Farra[14]. Wang and Kline[15] developed ray tracing based on Fermat's principle that can be applied to anisotropic materials. Ray tracing techniques based on Snell's law are less widely used due to the difficulty in finding the correct launch angle from the source that will assure termination at the appropriate receiver position. In addition, a dense fan of rays originating from each source is required to avoid the loss of information from low velocity zones. These concerns place immense computational demands on the method of ray tracing.

Matarese[16] implemented both ray tracing and tomographic inversion on a parallel machine, the nCUBE. Graph-theoretical ray tracing based on Moser's[12] shortest path technique was used together with the conjugate gradient back-projection method for the tomographic inversion. The code was written for a source domain decomposition as opposed to a matrix domain decomposition: each processor was assigned a source and performed the ray tracing and travel-time calculation corresponding to that source, followed by the calculation of the travel-time residual and the back-projection for the same source. Sullivan et al[17] also implemented the ray tracer and the tomographic inversion on a parallel machine, the Connection Machine. The ray tracer was based on Snell's Law and an algebraic reconstruction technique was used for the tomographic inversion. The work was completely parallel as all sources and receivers were considered simultaneously.

Several researchers developed algorithms to solve the acoustic wave propagation problem on parallel computers. Delsanto[18] et al presented a technique for the finite difference solution of wave propagation in a one-dimensional (later extended to two dimensions) homogeneous material using a Connection Machine. They have since refined the technique to model geometrically complex heterogeneous media (Delsanto[19], Schecter[20]). Vasco and Majer[21] presented a finite difference algorithm for wavefield computation on the CM2 processor. The resulting travel times were used in tomographic velocity reconstruction. Podvin and Lecomte[22] also used the CM2 processor to calculate a finite difference solution to the eikonal equation to compute travel-times in heterogeneous media.

A parallel algorithm for wave propagation allows an alternate approach to the tomography problem. The reconstruction of the full acoustic field to calculate travel-times incorporates beam skew and ray bending in the problem formulation. This eliminates the time-consuming ray-tracing step. Kline et al[23] used a finite-difference solution to the wave equation in the application of acoustic tomography to anisotropic media. Other approaches (Ammon and Vidale[24], Shuster and Quintus-Bosz[25]) calculated the finite difference solution of the eikonal equation and then back projected the ray paths using the method of steepest descent.

An additional advantage to the full-field approach is that the travel-times are a function of the material properties. This allows the determination of numerous material parameters especially in anisotropic composite materials. Kline and Wang[3] used this technique to determine the cure state of the matrix in a unidirectional fiber

composite. Other types of imperfections in fiber-reinforced composites are fiber misalignment and fiber waviness. These imperfections can develop as a result of manufacturing or in-service conditions. Wooh and Daniel[26] have developed a ray-tracing technique to detect fiber waviness in a composite. The method determines the pattern of fiber waviness, not a quantitative figure.

The present work tackles two problems. The first is to develop an algorithm for ray-based tomography that is completely parallel. Here, matrix domain decomposition is used where all the ray paths for all source-receiver pairs are considered simultaneously. The second is to use the full-field approach to determine not only the presence but also the amount of any rotation or buckling in an orthotropic composite laminate.

CHAPTER 2

THEROETICAL BACKGROUND

Numerous nondestructive testing techniques are used to test composite materials, such as ultrasonics, radiography and thermal imaging. Specifically, acoustic image reconstruction provides information about different parameters such as the stiffness, degree of matrix cure, and lay-up parameters of the composite. The anisotropic nature of the composite complicates ultrasonic testing due to the directional dependence of the velocity. The following sections discuss the nature of wave propagation in anisotropic materials and also the micromechanics of composite materials.

2.1 Wave propagation in anisotropic media

The governing equations for elastic waves in anisotropic media are derived from the dynamic equilibrium equations of linear elasticity. Neglecting body forces, these equations are

$$\rho \ddot{u}_i = \sigma_{ij,J} \tag{2.1}$$

Substituting the stress-strain relations for a linear elastic material

$$\rho \ddot{u}_i = \left(C_{ijkl} \varepsilon_{kl} \right)_j \tag{2.1}$$

The strains can be written in terms of displacements

$$\varepsilon_{kl} = \frac{1}{2}\left(u_{k,l} + u_{l,k} \right). \tag{2.2}$$

Assuming that the stiffness matrix is independent of position, one can express the wave equation as

$$\rho \ddot{u}_i = C_{ijkl} u_{k,lj} \quad . \tag{2.3}$$

The above equation describes the wave propagation through a linear elastic material in three dimensions. Assuming a harmonic plane wave solution to the wave equation

$$u_i = A_o \alpha_i e^{i(kl_i x_i - \omega t)} \tag{2.4}$$

and then differentiating with respect to time results in

$$\ddot{u}_i = \omega^2 A_o \alpha_i e^{i(kl_i x_i - \omega t)} \quad . \tag{2.5}$$

where: A_o = displacement amplitude

α = polarization vector

k = wave number

l = direction of propagation or wave normal

ω = frequency

Substitution of the plane wave solution for the displacement into the wave equation results in the Christoffel equation

$$\left(C_{ijkl} l_j l_l - \rho V^2 \delta_{ik}\right)\alpha_k = 0 \tag{2.6}$$

where: V = phase velocity = ω/k

This is an eigenvalue problem where the eigenvalues, ρV^2, correspond to the phase velocities of the material and the eigenvectors, α_k, represent the three directions of polarization. The eigenvalues or phase velocities are found by setting the determinant of the above equation equal to zero and solving the set of simultaneous equations.

$$\left|\lambda_{ik} - \rho V^2 \delta_{ik}\right| = 0 \tag{2.7}$$

In the above equation, $\lambda_{ik} = C_{ijkl}\, l_j l_l$ and is known as the Christoffel tensor. The phase velocities are used to determine the stiffness matrix for a given material.

For an isotropic material, the first eigenvalue corresponds to the longitudinal velocity and the corresponding eigenvector, i.e. the polarization vector, is in the same direction as the wave normal.

$$\vec{\alpha} \cdot \vec{l} = 1 \tag{2.8}$$

The other two eigenvalues are a common root and correspond to the shear velocity. Here, the eigenvectors and the direction of propagation are perpendicular to the wave normal.

$$\vec{\alpha} \cdot \vec{l} = 0 \tag{2.9}$$

For an anisotropic material, the above relationships between the polarization vectors and the wave normal generally do not hold. The direction of the particle displacement and the wave normal are not either exactly parallel or perpendicular. In general, if

$$\vec{\alpha}_i \cdot \vec{l} = \max\left\{\vec{\alpha}_1 \cdot \vec{l}, \vec{\alpha}_2 \cdot \vec{l}, \vec{\alpha}_3 \cdot \vec{l}\right\} \tag{2.10}$$

the wave is considered quasi-longitudinal. Otherwise the wave is considered quasi-transverse. It should be noted that in all cases, since the polarization vectors are eigenvectors, they form an orthogonal set with respect to each other.

The energy flux vector also is not aligned with the wave normal for an anisotropic material. The energy flux is defined as the transport of energy across the wave front. This energy is what is detected by sensors during ultrasonic measurements. There is an important distinction between energy or group velocity and the phase velocity. The energy is measured experimentally, while the phase velocity is used to calculate material properties.

2.2 Energy Propagation

The total energy in a given volume of material is defined as the sum of the kinetic energy, W, and the potential energy, Φ.

$$\begin{aligned} E &= \int_V [W + \Phi] dv \\ E &= \int_V \left[\tfrac{1}{2}\rho \dot{u}_i^2 = \tfrac{1}{2}\sigma_{ij}\varepsilon_{ij}\right] dv \end{aligned} \tag{2.11}$$

The transport of energy across the wave front can be defined as the rate of change of the total energy in the volume. Taking the derivative of both sides of the above integral, the propagation of energy across the wave front can be described as

$$\frac{dE}{dt} = \int_V \left[\frac{\partial}{\partial t}\left(\tfrac{1}{2}\rho \dot{u}_i^2\right) + \frac{\partial}{\partial t}\left(\tfrac{1}{2}\sigma_{ij}\varepsilon_{ij}\right)\right] dv \tag{2.12}$$

The time derivative of the potential energy can be found using the chain rule and using equation (2.2) to substitute the displacements for strain.

$$\frac{\partial \Phi}{\partial t} = \frac{\partial \Phi}{\partial \varepsilon} \cdot \frac{\partial \varepsilon}{\partial t} = \sigma_{ij} \dot{u}_{i,j} \tag{2.13}$$

Since by definition

$$\left(\sigma_{ij} \dot{u}_i\right)_{,j} = \sigma_{ij} \dot{u}_{ij,j} + \sigma_{ij,j} \dot{u}_i \tag{2.14}$$

the equation for energy propagation can be written as

$$\begin{aligned} \frac{dE}{dt} &= \iint_V \left[\rho \dot{u}_i \ddot{u}_i + \left(\sigma_{ij} \dot{u}_i\right)_{,j} - \sigma_{ij,j} \dot{u}_i\right] dv \\ \frac{dE}{dt} &= \iint_V \left[\left(\rho \ddot{u}_i - \sigma_{ih,j}\right) \dot{u}_i\right] dv - \iint_V \left[\left(\sigma_{ij} \dot{u}_i\right)_{,j}\right] dv \end{aligned} \tag{2.15}$$

However, the equation of motion for a continuum

$$\rho \ddot{u}_i = \sigma_{ij,j} \tag{2.16}$$

requires that the first integral vanish, leaving,

$$\frac{dE}{dt} = \iint_V \left[\left(\sigma_{ij} \dot{u}_i\right)_{,j}\right] dv . \tag{2.17}$$

Using the divergence theorem to convert the volume integral to a surface integral results in

$$\begin{aligned} \frac{dE}{dt} &= \int_S \sigma_{ij} \dot{u}_i n_j ds \\ \frac{dE}{dt} &+ \int_S P_j n_j ds = 0 \\ \text{where:} \quad P_j &= -\sigma_{ij} \dot{u}_i \end{aligned} \tag{2.18}$$

The vector P_j is defined as the energy flux vector. It represents the flow or the flux of energy crossing the wave front.

The acoustic tomography algorithm is computationally intensive. There is a significant computational advantage in reducing a three-dimensional problem to a two-dimensional problem. This computational short cut is allowed if the energy flux vector remains in the same plane as the two-dimensional wave propagation used for calculation in the tomography algorithm. The following section demonstrates that the energy flux vector for an orthotropic material arbitrarily rotated about the *z*-axis remains in plane.

The energy vector can be written as

$$P_j = -\sigma_{ij}\dot{u}_i = -C_{ijkl}u_{k,l}\dot{u}_i \tag{2.19}$$

Using a plane wave solution for the displacement

$$u = A_\circ \alpha_i \cos(\omega t - kl_m x_m) \tag{2.20}$$

and substituting the spatial and time derivatives for the displacement

$$\begin{aligned} u_{k,l} &= -A_\circ k l_l \alpha_k \sin(\omega t - kl_m x_m) \\ \dot{u}_i &= -A_\circ \omega \alpha_k \sin(\omega t - kl_m x_m) \end{aligned} \tag{2.21}$$

into the equation for the energy flux vector equation results in

$$\begin{aligned} P_j &= C_{ijkl} l_l \alpha_i \alpha_k k\omega A_\circ^2 \sin^2(\omega t - kl_m x_m) \\ P_j &= C_{ijkl} l_l \alpha_i \alpha_k \gamma \end{aligned} \tag{2.22}$$

where: $\gamma = A_\circ^2 k\omega \sin^2(\omega t - kl_m x_m)$

The next step requires the C_{ijkl} matrix for an orthotropic material rotated around the z-axis. This is found by the tensor transformation

$$C'_{abcd} = a_{ai} a_{bj} a_{ck} a_{dl} C_{ijkl} \tag{2.23}$$

where the a matrix defines the direction cosines corresponding to the coordinate rotation. Using the standard contracted index notation,

$$\begin{aligned} 11 &\rightarrow 1 \quad 22 \rightarrow 2 \quad 33 \rightarrow 3 \\ 23 &\rightarrow 4 \quad 13 \rightarrow 5 \quad 12 \rightarrow 6 \end{aligned} \tag{2.24}$$

the C_{ijkl} matrix after rotation is,

$$\begin{bmatrix} C_{11} & C_{12} & C_{13} & 0 & 0 & C_{16} \\ C_{12} & C_{22} & C_{23} & 0 & 0 & C_{26} \\ C_{13} & C_{23} & C_{33} & 0 & 0 & C_{36} \\ 0 & 0 & 0 & C_{44} & C_{45} & 0 \\ 0 & 0 & 0 & C_{45} & C_{55} & 0 \\ C_{16} & C_{26} & C_{36} & 0 & 0 & C_{66} \end{bmatrix} \tag{2.25}$$

For an incident wave in the 1-2 plane, the wave normal, l, is

$$l = \begin{pmatrix} \sin\phi \\ \cos\phi \\ 0 \end{pmatrix} \tag{2.26}$$

It can be shown that the third component of the polarization vector, or α, is also zero. The polarization vector is found from the Christoffel equation.

$$\left(C_{ijkl} l_j l_l - \rho\ V^2 \delta_{ik}\right)\ \alpha_k\ =\ 0 \tag{2.27}$$

The Christoffel equation constitutes an eigenvalue problem with eigenvectors α_k that represent the polarization of a propagating wave. Since the third component of the wave normal, l, is equal to zero, the Christoffel equation becomes

$$\begin{bmatrix} \lambda_{11} - \rho\ v^2 & \lambda_{12} & 0 \\ \lambda_{12} & \lambda_{22} - \rho\ v^2 & 0 \\ 0 & 0 & \lambda_{33} - \rho\ v^2 \end{bmatrix} \begin{bmatrix} \alpha_1 \\ \alpha_2 \\ \alpha_3 \end{bmatrix} = 0 \tag{2.28}$$

where $\lambda_{ik} = C_{ijkl} l_j l_l$

The first two eigenvalues represent the quasi-longitudinal and the quasi-shear wave, and the third component of these eigenvectors is zero. The third eigenvalue is equal to (λ_{33} - ρv^2) and its corresponding eigenvector is the unit vector in the third direction.

$$\alpha_A=\begin{pmatrix}\alpha_{A1}\\ \alpha_{A2}\\ 0\end{pmatrix} \quad \alpha_B=\begin{pmatrix}\alpha_{B1}\\ \alpha_{B2}\\ 0\end{pmatrix} \quad \alpha_C=\begin{pmatrix}0\\ 0\\ 1\end{pmatrix} \tag{2.29}$$

If either of the first two eigenvectors is used in the energy flux equation, the indices representing the third component are eliminated. Since the third component of the wave normal is equal to zero, the *l=3* index is also eliminated from the energy flux equation.

$$P_j = C_{ijkl} l_l \alpha_i \alpha_k \gamma \quad l \neq 3, k \neq 3, i \neq 3 \tag{2.30}$$

In order for the energy flux vector to remain in the 1-2 plane for the two dimensional solution, the third component or P_3 must be equal to zero. The third component of the energy flux vector can be written as

$$\begin{aligned} P_3=(&C_{1311} l_1 \alpha_1 \alpha_1 + C_{1312} l_2 \alpha_1 \alpha_1 + C_{1321} l_1 \alpha_1 \alpha_2 + C_{1322} l_2 \alpha_1 \alpha_2 + \\ &C_{2311} l_1 \alpha_2 \alpha_1 + C_{2312} l_2 \alpha_2 \alpha_1 + C_{2321} l_1 \alpha_2 \alpha_{21} + C_{2322} l_2 \alpha_2 \alpha_2)\gamma \end{aligned} \tag{2.31}$$

The stiffness matrix components in the above equation are all zero, even after an arbitrary rotation, so the third component of the energy flux vector is also zero. Therefore, a two-dimensional approach to the problem is appropriate. The energy from an incident wave in the *1-2* plane remains in the *1-2* plane for the quasi-longitudinal wave and for one of the quasi-shear waves.

2.3 *Composite Materials*

Composite materials are composed of two or more different constituent materials, such as carbon fiber and an epoxy matrix. The combination of such materials results in an overall material that is well suited for specific purposes. Composites can be designed to improve the strength and stiffness of a structure, while maintaining low weight. The manufacture of composites, while improving the properties of the material, may also increase the complexity. Composites are usually macroscopically anisotropic materials, their properties dependent on orientation. The characterization of laminated fiber-reinforced composites will be discussed in this section.

A fiber-reinforced laminated composite consists of layers of unidirectional fibers or woven fibers in a matrix. The fiber orientation of each individual layer or lamina is varied. The anisotropy of these composites is introduced by the reinforcing fibers. For individual laminae, the stiffness of the material is greatest in the direction of the fiber and decreases as the direction becomes perpendicular to the fiber. The stacking sequence of the laminae also influences the mechanical properties of the composite, often introducing coupling of normal and shear stresses. In addition, a non-symmetric lay-up of the laminate can result in coupling between bending and extension.

For each lamina, the distribution of the fibers may be considered random and macroscopically uniform in the plane perpendicular to the fiber direction. In this plane only, the material properties of the laminae are independent of direction. The

laminae are defined as transversely isotropic. A transversely isotropic material requires five independent elastic moduli to characterize the material, whereas only two are needed for an isotropic material. If the fibers are layered evenly or form a pattern, the composite is orthotropic and requires nine independent elastic moduli for characterization. The stress-strain relationship for an orthotropic composite when the fibers are orientated with the coordinate axes is

$$\begin{Bmatrix} \sigma_{11} \\ \sigma_{22} \\ \sigma_{33} \\ \tau_{23} \\ \tau_{31} \\ \tau_{12} \end{Bmatrix} = \begin{bmatrix} C_{11} & C_{12} & C_{13} & 0 & 0 & 0 \\ C_{12} & C_{22} & C_{23} & 0 & 0 & 0 \\ C_{13} & C_{23} & C_{66} & 0 & 0 & 0 \\ 0 & 0 & 0 & C_{44} & 0 & 0 \\ 0 & 0 & 0 & 0 & C_{55} & 0 \\ 0 & 0 & 0 & 0 & 0 & C_{66} \end{bmatrix} \begin{Bmatrix} \varepsilon_{11} \\ \varepsilon_{22} \\ \varepsilon_{33} \\ \gamma_{23} \\ \gamma_{31} \\ \gamma_{12} \end{Bmatrix} \tag{2.32}$$

There is no interaction between normal stresses and shear strains or between shear stresses and normal strains. This is not the case when the fibers have been rotated and are no longer aligned with the coordinate axes.

In most structural applications, thin laminates are loaded in the plane of the laminate. Thus, the laminae can be considered to be under a condition of plane stress. The specially orthotropic (aligned with coordinate axes) stress-strain relations reduce to

$$\begin{Bmatrix} \sigma_{11} \\ \sigma_{22} \\ \tau_{12} \end{Bmatrix} = \begin{bmatrix} Q_{11} & Q_{12} & 0 \\ Q_{12} & Q_{22} & 0 \\ 0 & 0 & Q_{66} \end{bmatrix} \begin{Bmatrix} \varepsilon_{11} \\ \varepsilon_{22} \\ \gamma_{12} \end{Bmatrix} \tag{2.33}$$

The Q_{ij} are the reduced stiffnesses and are related to the C_{ij} matrix stiffness components by

$$Q_{ij} = C_{ij} - \frac{C_{i3}C_{j3}}{C_{33}} \qquad (i,j) = 1,2,6 \tag{2.34}$$

When the composite is rotated so that the principal direction (fiber direction) of the material no longer coincides with a coordinate direction, a tensor transformation of the stresses and strains is required. The transformation equations for a rotation of angle θ about the z coordinate axis are

$$\begin{Bmatrix} \sigma'_{11} \\ \sigma'_{22} \\ \tau'_{12} \end{Bmatrix} = \begin{bmatrix} \cos^2\theta & \sin^2\theta & -2\sin\theta\cos\theta \\ \sin^2\theta & \cos^2\theta & 2\sin\theta\cos\theta \\ \sin\theta\cos\theta & -\sin\theta\cos\theta & \cos^2\theta \end{bmatrix} \begin{Bmatrix} \sigma_{11} \\ \sigma_{22} \\ \tau_{12} \end{Bmatrix}$$
$$\begin{Bmatrix} \varepsilon'_{11} \\ \varepsilon'_{22} \\ \frac{\gamma'_{12}}{2} \end{Bmatrix} = \begin{bmatrix} \cos^2\theta & \sin^2\theta & -2\sin\theta\cos\theta \\ \sin^2\theta & \cos^2\theta & 2\sin\theta\cos\theta \\ \sin\theta\cos\theta & -\sin\theta\cos\theta & \cos^2\theta \end{bmatrix} \begin{Bmatrix} \varepsilon_{11} \\ \varepsilon_{22} \\ \frac{\gamma_{12}}{2} \end{Bmatrix} \tag{2.35}$$

The above equations can be written more compactly as

$$\{\sigma'\} = [T]^{-1}\{\sigma\}$$
$$\{\varepsilon'\} = [T]^{-1}\{\varepsilon\} \tag{2.36}$$

To avoid the complication of the strain tensor, the Reuter[27] matrix is used.

$$\begin{Bmatrix} \varepsilon_{11} \\ \varepsilon_{22} \\ \gamma_{12} \end{Bmatrix} = \begin{bmatrix} 1 & 0 & 0 \\ 0 & 1 & 0 \\ 0 & 0 & 2 \end{bmatrix} \begin{Bmatrix} \varepsilon_{11} \\ \varepsilon_{22} \\ \frac{\gamma_{12}}{2} \end{Bmatrix} \quad \text{or} \quad \begin{Bmatrix} \varepsilon_{11} \\ \varepsilon_{22} \\ \frac{\gamma_{12}}{2} \end{Bmatrix} = [R]^{-1} \begin{Bmatrix} \varepsilon_{11} \\ \varepsilon_{22} \\ \gamma_{12} \end{Bmatrix} \tag{2.37}$$

Now the stress-strain relations for the rotated system can be written as

$$\{\sigma'\} = [Q']\{\varepsilon'\}$$
$$[T]^{-1}\{\sigma\} = [Q'][T]^{-1}[R]^{-1}\{\varepsilon\} \tag{2.38}$$
$$\{\sigma\} = [T][Q'][R][T]^{-1}[R]^{-1}\{\varepsilon\}$$

However,

$$\{\sigma\} = [Q]\{\varepsilon\} \tag{2.39}$$

Therefore,

$$[Q'] = [T]^{-1}[Q][R][T][R]^{-1} \tag{2.40}$$

According to Jones[28]

$$[R][T][R]^{-1} = [T]^{-T} \tag{2.41}$$

where the superscript –T indicates the inverse of the matrix transpose. Substituting equation (2.41) into equation (2.40) results in

$$[Q'] = [T]^{-1}[Q][T]^{-T} \tag{2.42}$$

The [Q`] reduced stiffness matrix relates the stresses and strains when the fiber direction of the composite is not aligned with the coordinate direction.

$$\begin{Bmatrix} \sigma'_{11} \\ \sigma'_{22} \\ \tau'_{12} \end{Bmatrix} = \begin{bmatrix} Q'_{11} & Q'_{12} & Q'_{16} \\ Q'_{12} & Q'_{22} & Q'_{26} \\ Q'_{16} & Q'_{26} & Q'_{66} \end{bmatrix} \begin{Bmatrix} \varepsilon'_{11} \\ \varepsilon'_{22} \\ \gamma'_{12} \end{Bmatrix} \tag{2.43}$$

There remain only four independent parameters, although the stiffness matrix contains nine non-zero elements. However there is coupling between the shear stress and the normal strains and between the normal stresses and the shear strains. A material exhibiting this behavior is called *generally orthotropic.*

A fiber-reinforced laminate consists of two or more layers bonded together. The fiber orientation of each lamina is rotated in a specific direction, resulting in a laminate capable of withstanding loads in several directions. The analysis of the laminate assumes a perfect, non shear-deformable bond between the lamina allows

continuous displacements across the lamina boundaries. In addition, it is assumed that the laminate is a thin structure. Because the stresses vary from lamina to lamina, it is more convenient to substitute resultant forces and moments for the stresses. Since the study of wave propagation in composite materials involves only normal and shear forces, the effect of applied bending moments on a laminate will not be discussed. Letting [N] represent normal forces per unit length, the force strain relations for a plate shaped laminate are

$$\{N\} = [A]\{\bar{\varepsilon}\} + [B]\{\kappa\} \tag{2.44}$$

where: $\bar{\varepsilon} \equiv$ midplane strain and $\kappa \equiv$ curvature.

$$\begin{aligned} [A] &= \sum_{k=1}^{N} [C]_k \ (z_k - z_{k-1}) \\ [B] &= \frac{1}{2} \sum_{k=1}^{N} [C]_k \ \left(z^2_k - z^2_{k-1}\right) \end{aligned} \tag{2.45}$$

The stiffness matrix [C] is defined for each layer k and is dependent of the fiber angle of each layer. The z coordinates of the upper and lower surfaces of each layer k are defined by z_{k-1} and z_k as shown in Figure 2.1

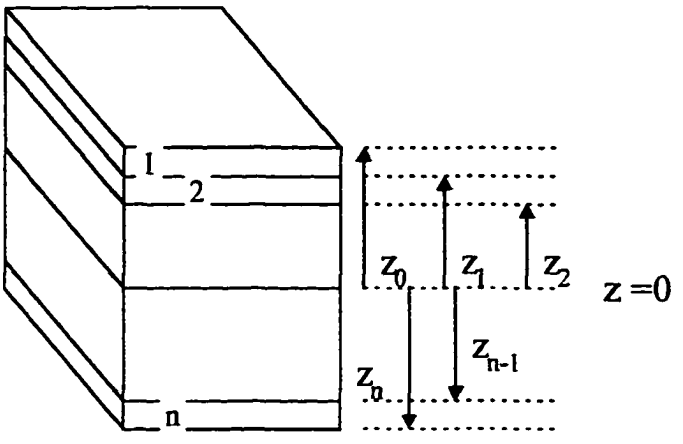


Figure 2.1 Geometry of a laminate.

If the [B] matrix is non-zero, there will be coupling between the normal forces and the bending and twisting of the laminate. This is in addition to the coupling of the normal stresses and the shear strains mentioned previously. However, if the laminate is symmetric about the mid-plane in both material properties and geometry, then the [B] matrix is zero. For simplicity, only symmetric laminates will be considered here.

Due to its simplicity, the quasi-isotropic laminate is of special interest. This is a symmetric laminate with usually a $[0/60/-60]_s$ or a $[0/\pm 45/90]_s$ laminae sequence. Since the laminate is symmetric, the [B] matrix is zero. Using equation (2.42) to calculate the [A] matrix and then applying the transformation equations for an arbitrary rotation, it can be shown that the in-plane stiffnesses are independent of direction, thus the nomenclature quasi-isotropic.

2.4 *Engineering Properties of Composite Materials*

In general, the engineering moduli or properties are experimentally measured, not the components of the C_{ij} matrix. For an orthotropic material, the relationship between the [C] matrix and the engineering constants are as follows

$$
\begin{aligned}
C_{11} &= \frac{1-\upsilon_{23}\upsilon_{32}}{E_2E_3\Delta} \\
C_{12} &= \frac{\upsilon_{12}+\upsilon_{32}\upsilon_{13}}{E_1E_3\Delta} \\
C_{13} &= \frac{\upsilon_{13}+\upsilon_{12}\upsilon_{23}}{E_1E_2\Delta} \\
C_{22} &= \frac{1-\upsilon_{13}\upsilon_{31}}{E_1E_3\Delta} \\
C_{23} &= \frac{\upsilon_{23}+\upsilon_{13}\upsilon_{21}}{E_2E_1\Delta} \\
C_{33} &= \frac{1-\upsilon_{12}\upsilon_{21}}{E_1E_2\Delta} \\
C_{44} &= G_{23} \\
C_{55} &= G_{31} \\
C_{66} &= G_{12}
\end{aligned}
\qquad (2.46)
$$

where: $$\Delta = \frac{1-\nu_{12}\nu_{21}-\nu_{23}\nu_{32}-\nu_{31}\nu_{13}-2\nu_{21}\nu_{32}\nu_{13}}{E_1E_2E_3}$$

For a plane stress problem the relations simplify

$$
\begin{aligned}
Q_{11} &= \frac{E_1^2}{E_1-\upsilon_{12}^2E_2} \\
Q_{12} &= \frac{\upsilon_{12}E_1E_2}{E_1-\upsilon_{12}^2E_2} \\
Q_{22} &= \frac{E_1E_2}{E_1-\upsilon_{12}^2E_2} \\
Q_{66} &= G_{12}
\end{aligned}
\qquad (2.47)
$$

The above equations can be used to find the [C] matrix for each fiber composite lamina, once the engineering constants for a fiber composite material are known. These can be found using a micromechanics of materials approach.

$$
\begin{aligned}
E_1 &= E_f V_f + E_m V_m \\
E_2 &= \frac{E_f E_m}{V_m E_f + V_f E_m} \\
\upsilon_{12} &= \upsilon_m V_m + \nu_f V_f \\
G_{12} &= \frac{G_m G_f}{V_m G_f + V_f G_m}
\end{aligned}
\tag{2.48}
$$

where: E_f = Young's modulus for an isotropic fiber

E_m = Young's modulus for an isotropic matrix material

G_f = The shear modulus for an isotropic fiber

G_m = The shear modulus for an isotropic matrix material

ν_f = Poisson's ratio for an isotropic fiber

ν_f = Poisson's ratio for an isotropic fiber

V_m = Volume fraction of the matrix

This approach is called the *rule of mixtures* and requires several simplifying assumptions:

1) Both the fiber and matrix are homogeneous, linearly elastic, and isotropic,
2) The lamina is macroscopically homogeneous and orthotropic, linearly elastic, and originally stress-free.
3) The bonds between the fibers and the matrix are perfect.

4) The strains in the fiber direction of the composite are the same in both the fiber and the matrix.

Higher accuracy may be obtained using an elasticity approach, such as bounding techniques, (Hashin and Rosen)[29] or the Halpin-Tsai[30]. The rule of mixtures is used for the study. Table 2.1 lists the fiber and matrix properties and a calculated orthotropic stiffness matrix.

Engineering Properties	Glass Fiber 60%	Epoxy Matrix 40%	Lamina
E_1	72.0 GPa	4.0 GPa	44.8 GPa
E_2	72.0 GPa	4.0 GPa	9.23 GPa
ν_{12}	0.25	0.37	0.298
ν_{21}	0.25	0.37	0.061
G_{12}	28.8 GPa	1.46 GPa	3.39 GPa

Table 2.1 Material Properties for a Glass/Epoxy Composite.

For a regular symmetric cross-ply laminate with a [0/90/0] lay-up, and laminae of equal thickness, the [A] matrix can be calculated using equation (2.42). Assuming a lamina thickness of 0.1 m, the [A] matrix is

$$[A] = \begin{bmatrix} 10.06 & 0.84 & 0 \\ 0.84 & 6.40 & 0 \\ 0 & 0 & 1.02 \end{bmatrix} \text{ GPa} \tag{2.46}$$

If there is some warpage of this laminate and the [0/90/0] sequence is rotated 5 degrees, the [A] matrix becomes

$$[A] = \begin{bmatrix} 9.95 & 0.92 & 0.62 \\ 0.84 & 6.40 & -0.30 \\ 0.62 & -.30 & 1.10 \end{bmatrix} \text{ GPa} \tag{2.47}$$

Since the laminate is symmetric, the [B] matrix is zero. Ultrasonic measurements are essentially an application of normal and or shear stresses to a boundary, therefore, bending and twisting are not concerns in a wave propagation problem. In this case, the [A] matrix can be used interchangeably with the Q_{ij} matrix.

Numerical simulations of ultrasonic measurements are incorporated in a tomographic algorithm in this study to determine the amount of rotation in a composite laminate. This can be used to identify manufacturing defects or misalignment in a composite laminate.

CHAPTER III

PARALLEL PROCESSING

The programs in this study were written for the Connection Machine, a massively parallel supercomputer made by Thinking Machines Corporation. The term "massive" implies multiple processors (CPUs) within one machine[31]. The Connection Machines used here are located at the Naval Research Lab in Washington, D.C. The tomographic inversion combined with the ray-tracing algorithm was written for the CM200 model, while the tomographic inversion combined with full-field wave propagation was written for the CM5 model.

The CM200 has 8192 independent processors, each with 128 Kbytes of memory. The CM200 is connected to a *front end* computer which manages interprocessor communication and stores and executes commands involving scalars or serial computations. The Naval Research Lab also has two CM5 machines. The *Starship* has 256 nodes, each with four vector units and 128 Mbytes of memory, and a 400 Gbyte disk array. The *Shuttlecraft* has 32 nodes, each with four vector units and 128 Mbytes of memory, and a 100 Gbyte disk array. The nodes on the CM5 are equivalent to the processors on the CM200 and the partition manager is functionally equivalent to the CM200 *front end* computer.

A computer with a parallel architecture is capable of performing simultaneous numerical operations on large data sets. An operation can be performed on an entire array at one time with a single command. For example, addition of two *nxn* arrays requires n^2 sequential operations on a serial machine. A single command conducts the same operation on all n^2 processors at once on a parallel machine. Applications may demand more individual processors then are physically available on a given machine. The virtual processors on a CM divide the local memory into as many regions as necessary. For example, if an application needs to simultaneously process one million pieces of data, $V=2^{20}$ virtual processors are requested. If the available hardware has $P=2^{16}$ physical processors, each processor must support $V/P=16$ virtual processors. This is known as the virtual-processor ratio or VP ratio. If the VP ratio is 16, then the virtual processor executes at a speed of 1/16 the speed of a physical processor[32].

The CM was designed to avoid the von Neumann bottleneck. This occurs when the total CPU time is dominated by the length of time to move data between processor and memory. There were two major design requirements; 1) include enough processors for real-life problem applications, with each processor having a relatively small amount of memory, and 2) hide the physical connectivity of the processors as thoroughly as the von Neumann computer hides the physical locality of memory[33]. In other words, configure the topology of the machine to match the topology of the problem.

A network was designed to provide interprocessor communication. Direct communication between every processor pair was impractical requiring $(10^6)^2$ switching points. Instead, a router system (switching elements wired in a sparse pattern) was developed. This system is analogous to the post office, taking a message from an individual home (processor) and sending it to a branch office, then a main office, followed by a different branch office and then to the intended recipient. To compensate for this cumbersome system, a second form of communication called NEWS (North, East, West, South) was added. It allows quick, direct communication between neighboring processors. Applications such as finite difference calculations, can exploit this NEWS relationship and significantly reduce computation time.

When an expression involves two or more arrays, the arrays must be conformable in shape and size in order to execute a parallel operation. For each group of parallel arrays, the CM configures a set of virtual processors into a logical grid that reflects the shape of the arrays and is allocated the same set of processors in the same order[34]. As a result, elemental operations on conformable arrays are extremely efficient. Each processor needs to look only within its own memory to locate the operands. Figure 3.1 highlights the memory of a single processor as the CM adds the corresponding elements of two arrays **A** and **B** and places the result in a third array **C**.

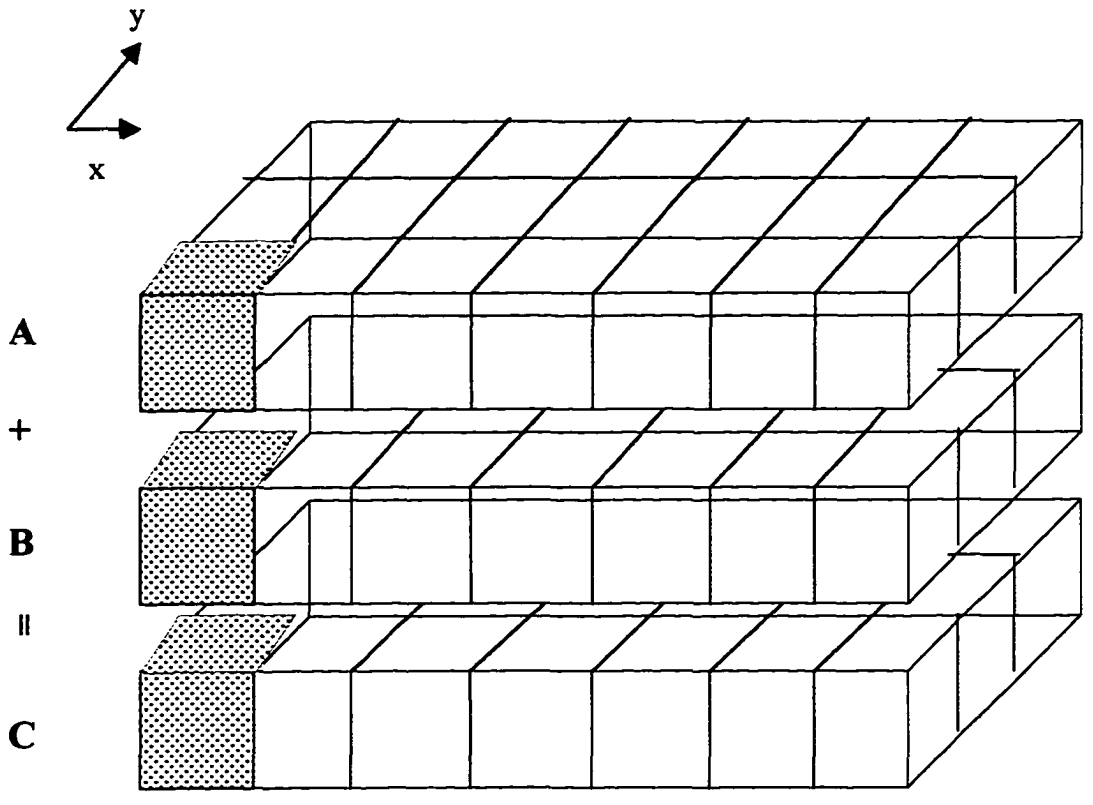


Figure 3.1 Matrix addition of two 3X7 arrays, A+B to form a third array, C. One processor is highlighted. NEWS communication is used.

The entire array operation is done in one step as each processor performs the elemental operation in synchrony. A serial machine requires a do-loop to perform this operation.

```
do  i =1 ,n
    do  j = 1,m
        C(i,j) = A(i,j)+B(i,j)
    end do
end do
```

The equivalent CM Fortran statement is

C=A+B

The CM Fortran language is as an implementation of Fortran 77 supplemented with array processing extensions from Fortran 90. Fortran 77 operates only on scalars. CM Fortran treats arrays as first-class objects that can be named in an expression or passed as an argument to an intrinsic function, where the operation is performed on every element in the array[33].

The key to efficient programming for the Connection Machine is the reduction in data movement. This includes maintaining a NEWS communication and avoiding serial operations on CM data arrays. A CM array is stored on the CM and data operations are performed in parallel. Scalars and serial arrays are stored on the *front end* computer. If an operation requires a single element from a CM array, it is transferred from the CM to the *front end* computer where the serial operation is performed and then returned to the CM. This data movement is time intensive and should be avoided at all cost.

3.1 Parallel Processing and Tomographic Reconstructions

Finite difference schemes and similar operations are well suited to parallel processing as they can be reduced to a series of matrix manipulations to go from time step to time step. The method is especially appealing for material studies. The material specimen can be divided into pixels corresponding to processors on the CM.

Different material properties can be assigned to each pixel and handled accordingly throughout the computations. For example, the wave equation

$$\rho \ddot{u} = C_{ijkl} u_{k,lj} \tag{2.3}$$

used in the tomographic reconstructions can be calculated using finite differences for the time and spatial derivatives. Each pixel is assigned a processor and has a specified C_{ijkl}. The spatial derivative is calculated using NEWS communication to exchange information with neighboring pixels or processors. The time derivative is calculated sequentially over three time steps.

The main difficulty encountered in adapting current tomographic imaging algorithms for parallel computation is in implementing the ray tracing. The ray tracing procedure requires velocity information from a $n \times m$ array representing the spatial grid to be used in calculations with $k \times l$ arrays that store the ray path information. These arrays are usually unconformable in size. In addition, the current spatial location must be accounted for without sequentially progressing through the spatial grid to maintain a strictly parallel operation.

These requirements can be met by using *vector-valued subscripts*. Vector-valued subscripts can be thought of as place-holders, used to associate the correct pixel velocity to each ray path, which is dependent on its current pixel location. In this ray tracing application two "place-holder" arrays are constructed, *ipost* and *jpost*. *Ipost* stores the current *i* (horizontal) position and *jpost* stores the current *j* (vertical) positions of each ray path. As each ray path enters a new spatial cell, these location arrays are updated. They are used to transform the $n \times m$ velocity array to a $k \times l$ array

by the use of vector valued subscripts. For example, let *vel* represent the *n x m* spatial velocity array. A new *k x l* sized array, v1, can be constructed by

$$v1(k,l) = vel\,[\,ipost(k,l)\,,\,jpost(k,l)\,]. \tag{3.1}$$

The *ipost* and *jpost* arrays identify the current spatial location of the ray path as it progresses through the specimen. For each spatial pixel that currently has a ray path traveling though it, the above statement transfers the velocity assigned to that pixel to a new array, v1. The new velocity array, v1, is conformable with any *k x l* sized array containing ray path information, such as the angle of the ray path. A similar array, v2, may be constructed using the subsequent pixel locations. This allows a Snell's law calculation of the incident angle for the next spatial cell, since the four arrays involved in the calculation are now conformable.

$$\frac{\sin(\alpha_{new})}{v2} = \frac{\sin(\alpha_{prev})}{v1} = c$$
$$\alpha_{new} = \sin^{-1}[\frac{v1}{v2}\sin(\alpha_{prev})] \tag{3.2}$$

The arrays α_{new} and α_{prev} contain the angle of incidence for each ray path. The arrays, *v1* and *v2* are the newly constructed velocity arrays that are conformable with α_{new} and α_{prev}. The progression of the ray path through the pixel grid is recorded for each ray path in this fashion. This progression is recorded simultaneously with the use of the vector-valued subscripts.

The ray-based tomographic reconstruction in this work uses matrix domain decomposition. All source-receiver pair calculations are performed simultaneously. The ray tracing method is a combination of Lytle and Dynes[7] and Langan et al[35]. An

algebraic reconstruction method is used for the tomographic inversion. In this case, the velocity of the material is reconstructed. This is the first known application of matrix domain parallel processing for this method of reconstruction. It allows numerous source-receiver pairs to be included in the model. The dense fan of rays originating from each source should eliminate the concern of caustics, which are associated with regions of little or no ray coverage.

The second tomographic reconstruction algorithm is based on acoustic wave propagation and was originally developed by Kline and Wang[3]. This algorithm does not require ray tracing and instead exploits the efficient NEWS communication of the CM5 with a finite difference calculation of the wave equation. The algorithm was changed to detect the rotation of individual pixels in a generally orthotropic material. Significant changes to the program were made to improve the parallelism, reducing the approximate CPU time from 20 hours to 1 hour.

The main roadblock to efficient parallelism in this algorithm is the perturbation of the reconstructed parameter. The angle of rotation for each pixel was perturbed slightly to construct the weighting factor for the tomographic correction factor. Each pixel must be perturbed individually, requiring a serial operation. Assigning the array a "home" on the front-end and restricting the array to serial operations can reduce the negative effect of this serial operation.

CHAPTER IV

RAY-BASED TOMOGRAPHIC RECONSTRUCTION

Two models were tested, a two-layer sample with a 50% velocity increase over one half of the sample and an Epstein layer with a gradual 50 % velocity increase over the entire sample. The source-receiver configurations were varied to test the boundary resolution. The speeds of the parallel and the serial computations were compared as the array size increased. Three major components comprised the tomographic algorithm; ray tracing, time delay calculations, and the tomographic inversion. The time delay calculations replaced experimental measurements in this numerical simulation.

4.1 Tomographic Inversion

Tomographic imaging is based on the fact that many experimentally measured quantities can be described as line integrals along the ray path. The measured time delay in an ultrasonic test is

$$T = \int_{source}^{receiver} \frac{1}{v(x,y)} ds \tag{4.1}$$

where v(x,y) represents the velocity of each point in a measurement plane. Algebraic reconstruction techniques, convolution methods, and Fourier domain reconstructions are commonly used to solve equation (4.1) for the desired material parameter (usually v(x,y)). This work used the simultaneous iterative reconstruction technique (SIRT), a variation of the algebraic reconstruction technique (ART).

ART is a series expansion technique where the specimen is divided into boxes or picture elements (pixels). Acoustic energy propagates through the pixels to provide a sum or projection of the pixel values. This approach differs from the transform methods where the specimen is considered to be continuous[35]. Figure 4.1 shows the discretization of a specimen into *n x m* pixels. The *kl*th ray path is directed from source *k* to receiver *l*. The length of ray path *kl* through pixel *ij* is denoted as a^{kl}_{ij}. The time delay for the *kl*th source-receiver pair is the accumulated time in the individual pixels intersected by this ray path.

$$T^{kl} = \sum_{i=1}^{n} \sum_{j=1}^{m} a_{ij}^{kl} s_{ij} \tag{4.2}$$

where: a^{kl}_{ij} = length of ray *kl* across pixel *ij*

s_{ij} = slowness (inverse of velocity) in pixel *ij*

T^{kl} = measured time delay for *kl*th ray path

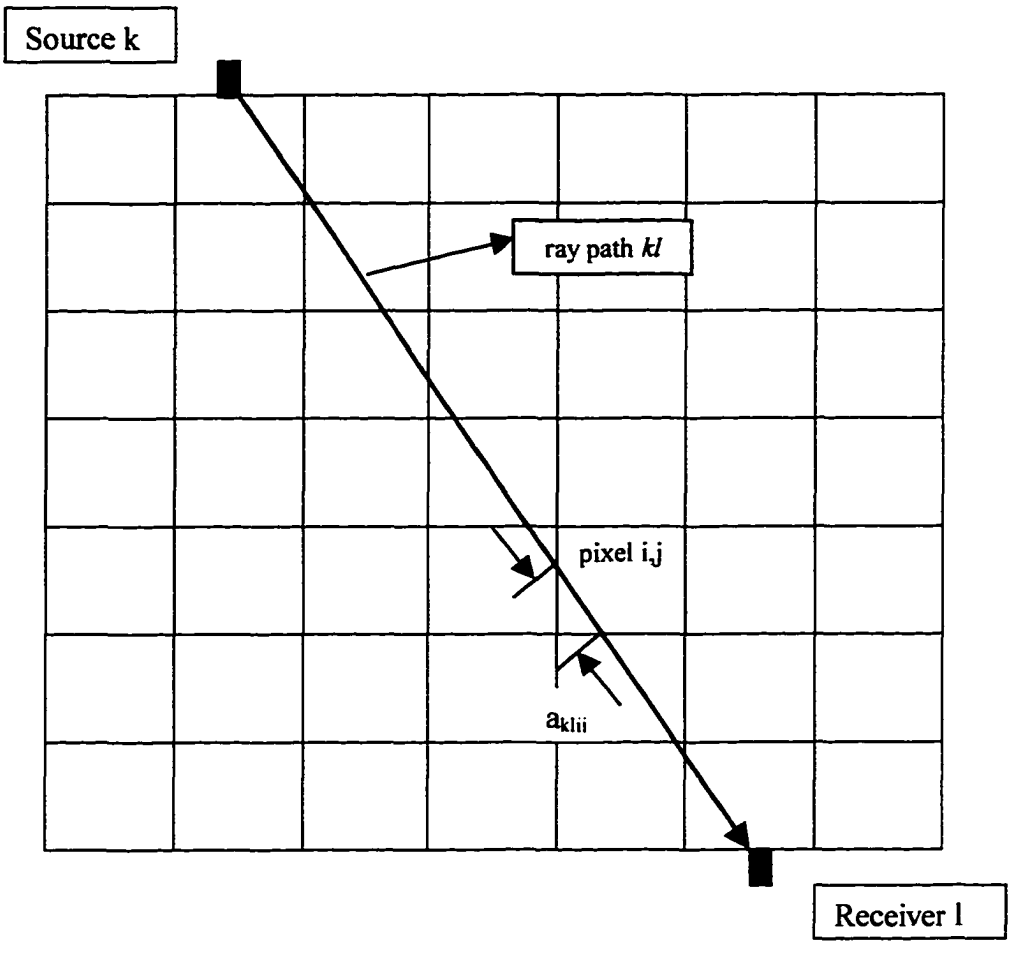


Figure 4.1 Illustration of model discretization. The length of the ray path *kl* across pixel *ij* is stored as a^{kl}_{ij}.

Equation (4.2) can be written in matrix form as

$$\vec{t} = [A]\vec{s} \tag{4.3}$$

The matrix [A] contains the ray path distance through each spatial cell in the sample. Due to the size of this matrix, direct methods of solving for the slowness vector are not practical. Since each ray intersects a small number of pixels, the [A] matrix is

sparse. For linear systems with large sparse matrices direct solution methods are inefficient. The CPU time is $O(mn^2)$ and the memory requirement is $O(mn)$.[36] In addition, experimental noise along with redundant or insufficient travel time data may preclude an exact solution. Iterative techniques, such as ART, are able to handle large numbers of equations, and since they are not exact methods, model and data errors are not as influential.

The ART algorithm adjusts the estimated slowness values in systematic fashion until the estimated time delays match the measured time delays. The change in slowness for each pixel is determined by the following procedure. The time delay estimation is

$$t^{kl} = \sum_{i=1}^{n} a_i^{kl} s_i^m . \tag{4.4}$$

In the above equation the subscript i indicates the pixel location and the subscript m represents the current iteration.

The difference between the time delay estimate and the measured time delay is

$$\Delta t^{kl} = T^{kl} - t^{kl} = T^{kl} - \sum_{i=1}^{n^2} a_i^{kl} \Delta s_i \tag{4.5}$$

where Δs_i represents the difference between the actual slowness and the estimated slowness. In order to eliminate the time delay difference, Δt^{kl}, the above equation must be solved for Δs_i. Requiring that the magnitude of the slowness change for each pixel be minimized results in the following solution for Δs_i.

$$\Delta s_i = \frac{\Delta t^{kl} a_i^{kl}}{\left(\sum_{i=1}^{n^2} a_i^{kl} \right)^2} \tag{4.6}$$

This is the standard slowness update for the ART algorithm. For each source-receiver pair the estimated time delay is calculated and equation (4.6) is applied to each pixel in the computation grid. This constitutes a single iteration. The procedure

$$s_i^{m+1} = s_i^m + \Delta s_i^m \tag{4.7}$$

is repeated until the calculated time delays match the measured time delays or are within a specified tolerance. An artificial damping factor, $0<\lambda>1$, may be added to improve the convergence of the solution.

$$s_i^{m+1} = s_i^m + \lambda \Delta s_i^m \tag{4.8}$$

4.2 Parallel Tomographic Inversion

The ART algorithm described in the preceding section is designed to examine the time delays from each individual ray and update the velocities before calculating the next ray. This is less then satisfactory for parallel reconstructions where all ray path data are available simultaneously. Instead a SIRT (Simultaneous Iterative Reconstructive Technique) algorithm is applied. The standard SIRT algorithm sums the slowness change for all the ray paths for each pixel and divides by the number of ray paths crossing that pixel[34].

$$\Delta \mathbf{S}_i = \frac{1}{N} \sum_k \sum_l \Delta s_i \tag{4.9}$$

where: N = the number of ray paths crossing pixel I

k,l = source-receiver pairs

Δs_i = the slowness change calculated using equation (4.8)

In this work, a weighted average was used for the correction factor. Proportionally greater weight is accorded rays whose pixel transit times are large in comparison to rays that spend only a short time in that particular cell. The weighted correction factor is given by

$$\Delta \mathbf{S}_i = \frac{\sum_k \sum_l \left(T^{kl} \Delta s_i \right)}{\sum_k \sum_l T^{kl}} \tag{4.10}$$

This correction was applied to all pixels simultaneously, avoiding a serial do-loop through the pixel grid.

4.3 Ray Tracing

In a heterogeneous medium the ray path lengths through each pixel are additional unknowns. A separate iterative technique is required to solve for the ray paths. The estimated slownesses are used to determine the ray paths. The most common ray-tracing techniques are based on Snell's Law or Fermat's principle of least time. These techniques require the solution of sets of ordinary differential equations.

Another technique introduced by Telford[38] and refined by Langan et al[35] is based on Snell's Law and a geometric type solution.

The ray-tracing method used here is an extension of the method of Langan[35] et al. They developed a ray-tracing model using a linear velocity gradient to represent a layered geologic formation. As the ray path enters the next layer, a geometric solution to Snell's Law is used to calculate the refracted angle of the ray path. This method is adjusted to allow velocity variations in the horizontal as well as vertical directions. Since each pixel is assumed to have homogeneous material properties, the linear velocity gradient within each pixel is changed to a constant velocity.

Figure 4.2 shows two rays from a single source traveling through four pixels. As the rays pass through a single pixel they can either exit through the bottom of the

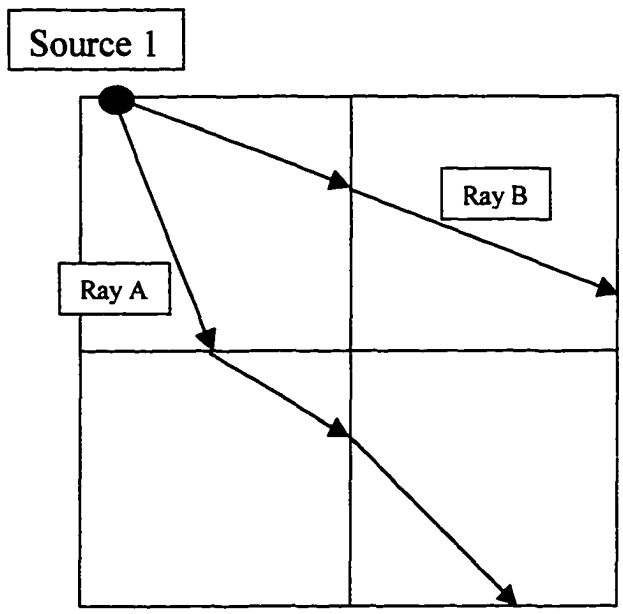


Figure 4.2 Ray paths traveling through heterogeneous media.

pixel or the side. The program checks every ray path to see if the ray path exits through the side or bottom of the pixel. This is done by first assuming the ray exits through the bottom of the pixel and then checking the length of the base of the triangle the ray path makes with the vertical. If this distance is greater then the distance from the source to the side edge of the pixel, then ray must exit the pixel through the side of the pixel.

Figure 4.3 depicts the procedure for a single pixel. The initial x,y coordinates of the ray and the ray angle, θ, are known. It is first assumed that the ray path will exit the pixel at the bottom edge. In that case the new x position will be x + x* or x + x**

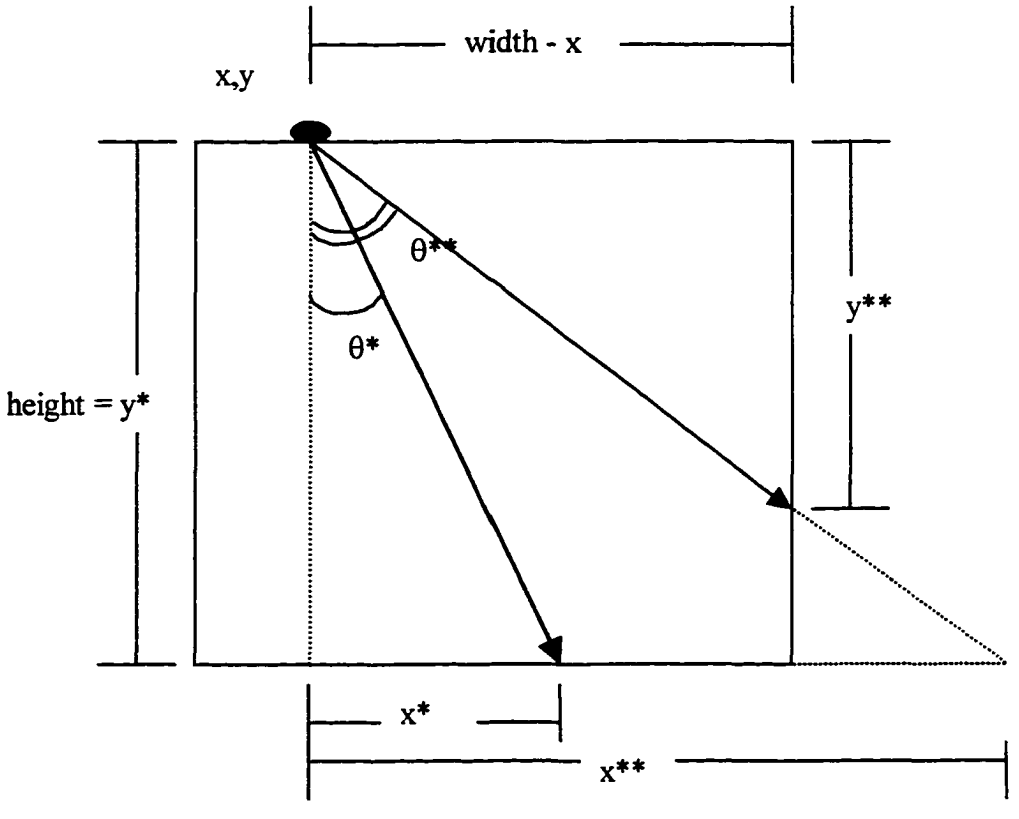


Figure 4.3 Illustration of geometric ray tracer.

and the new y position is y+y*. The next step is to check if the new x position is still within the pixel. If x+x** is greater then the width of the cell, the ray must exit through the side of the pixel. In this case, the new x position is now the side edge of the pixel and the y position is y+y. The lengths x* and y* are calculated using trigonometric identities. The length of the ray path across the pixel is calculated by

$$a_{ij}^{kl} = \sqrt{(x^2 + y^2)} \tag{4.11}$$

The ray path lengths, a^{kl}_{ij}, are used in the tomographic inversion, equation (4.8). Snell's Law determines the incident angle for the ray path in the subsequent pixel and the progression of the ray path is calculated by the following equation.

$$\frac{\sin\theta_i}{v_i} = \frac{\sin\theta_{i+1}}{v_{i+1}} \tag{4.12}$$

where: θ_i = ray path angle in current pixel

θ_{i+1} = ray path angle in the subsequent pixel

v_i = velocity in the current pixel

v_{i+1} = velocity in the subsequent pixel.

In summary, the ray-tracing procedure starts with known launch angles and x,y coordinates. The x,y coordinates for the subsequent pixel are calculated geometrically. The updated velocities are used in Snell's Law to determine the ray path angle in the next pixel. Since each pixel has a constant velocity, the ray path is a straight line through the pixel and the length is easily calculated using equation (4.10). The procedure is repeated until the end of the specimen is reached.

4.4 Ray Tracing in Parallel

As the complexity of a tomographic reconstruction increases, the number of ray paths required increases dramatically. A grid with a 100 x 100 pixels where every pixel on the outer edge has a source and receiver will have 12 x 100 x 100 ray paths. At least 100 pixel-to-pixel progressions through the grid are required for one parallel ray tracing iteration. A serial ray tracing iteration would require 100 x 100 pixel-to-pixel progressions for each of the 12 x 100 x 100 ray paths. A simultaneous, parallel ray tracing calculation can reduce computation time significantly. A program was written for the Connection Machine that tracks the propagation and calculates the length of all the rays across each pixel simultaneously.

As described in Chapter 3, the key to converting the ray-tracing program to a parallel platform is relating the spatial array that stores the pixel velocities to the "ray" arrays that store the ray path angle and the current coordinate positions. These arrays are not conformable in size or shape and vector-valued subscripts are required to overcome this problem. Figure 4.4 shows a 4 x 4 pixel grid with the stored velocity data. There are eight source-receiver pairs and the ray path angle and coordinate location are stored in 8 x 4 "ray" arrays.

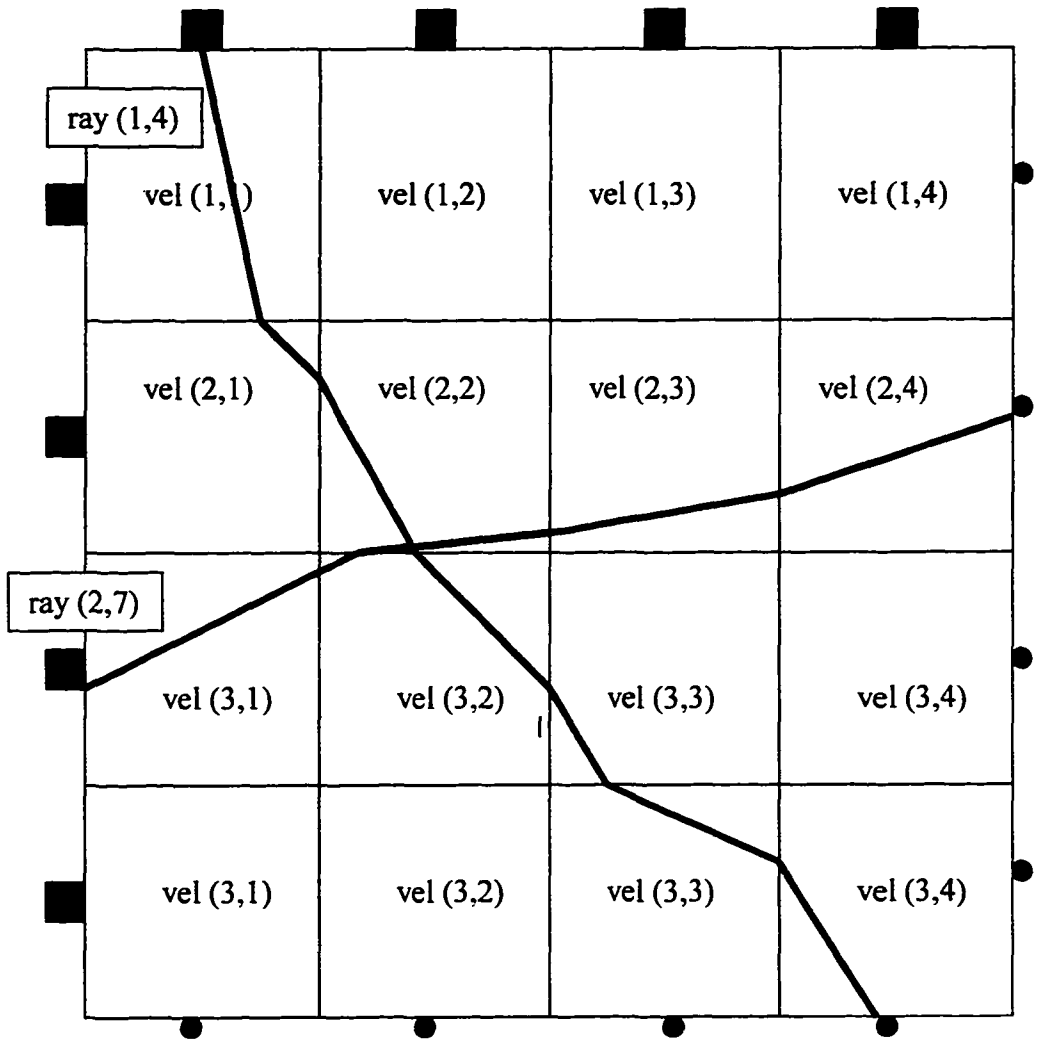


Figure 4.4 Pixel grid (4 x 4) with stored velocity information. The ray path angle and ray path locations are stored in 8 x 4 arrays, corresponding to the eight source-receiver pairs.

In order to perform the Snell's Law calculation in parallel, the velocities are transformed into a "ray" sized array by the use of vector-valued subscripts. When the velocity array and ray path angle arrays are conformable, Snell's Law is used to calculate the ray path angle in the subsequent pixels.

$$\frac{\sin(\alpha_{new})}{v2} = \frac{\sin(\alpha_{prev})}{v1} = c$$
$$\alpha_{new} = \sin^{-1}[\frac{v1}{v2}\sin(\alpha_{prev})] \tag{3.2}$$

The distances for each ray path are calculated simultaneously and stored in a four-dimensional array to be used later in the tomographic inversion. It is necessary to store a value for the length of each ray path across every pixel. This is a limiting factor in this program, due to memory requirements.

4.5 Time Delay Calculations

The tomographic reconstruction algorithm requires a calculation of the time delay. The time delay data are calculated using a Snell's Law formulation. The ray path distances are divided by the cell velocities and summed over the entire ray for each source-receiver pair. The data from each source-receiver pair are compared to the measured time delay data.

A common problem in the inversion procedure is that the launch angles necessary to match source locations to specified receiver positions are unknown. Generally the shooting method is used to overcome this problem. The shooting method changes what is essentially a boundary value problem to an equivalent initial

value problem[39]. The shooting method starts with an initial guess for the launch angle. The ray-tracing procedure is performed and the ray termination point is compared to the specified receiver position. A second guess for the launch angle is made and the ray-tracer is run again. Assuming the relationship between the receiver position and the launch angle is linear, the data from the two previous calculations can be used in an interpolation to determine the correct launch angle. A third and final ray tracing is performed and the data from this run are sent to the tomographic algorithm.

The ray-tracer is the most CPU intensive portion of the entire algorithm. A method was developed to avoid the costly repetition of this procedure. A polynomial approximation to the time delay curve replaces the specific source-receiver time delay measurements. In a separate program a polynomial expression is found to fit the time delay curve using a least square regression. This expression is input into the tomography program. Determination of specific launch angles is no longer required, since the polynomial expression can calculate a measured time delay regardless of where the ray terminates. As a result, only one iteration of the ray tracing procedure is required for each tomographic iteration. The time delay curve for a single source is shown in Figure 4.5 (a).

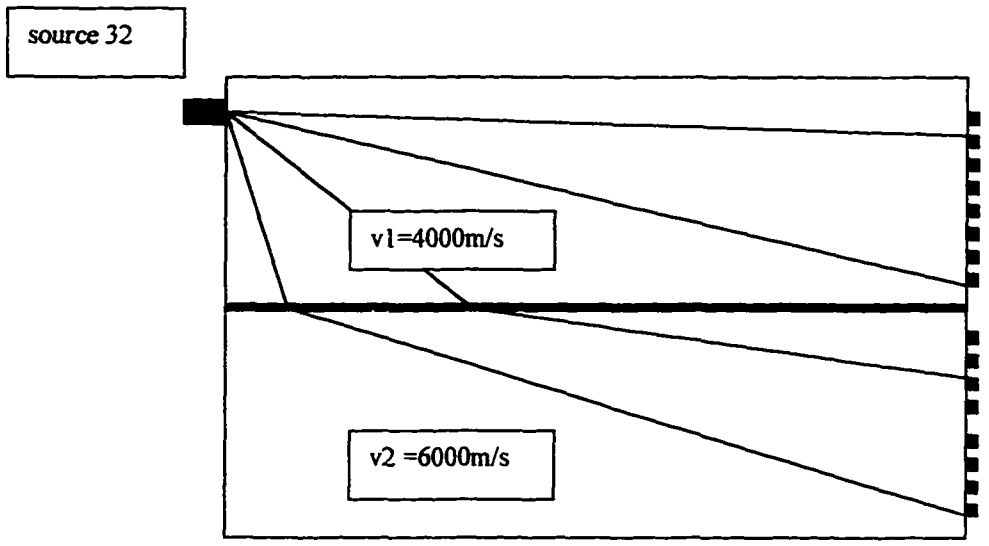


Figure 4.5 (a) Rays propagating from a single source on upper left side of a two-layer model.

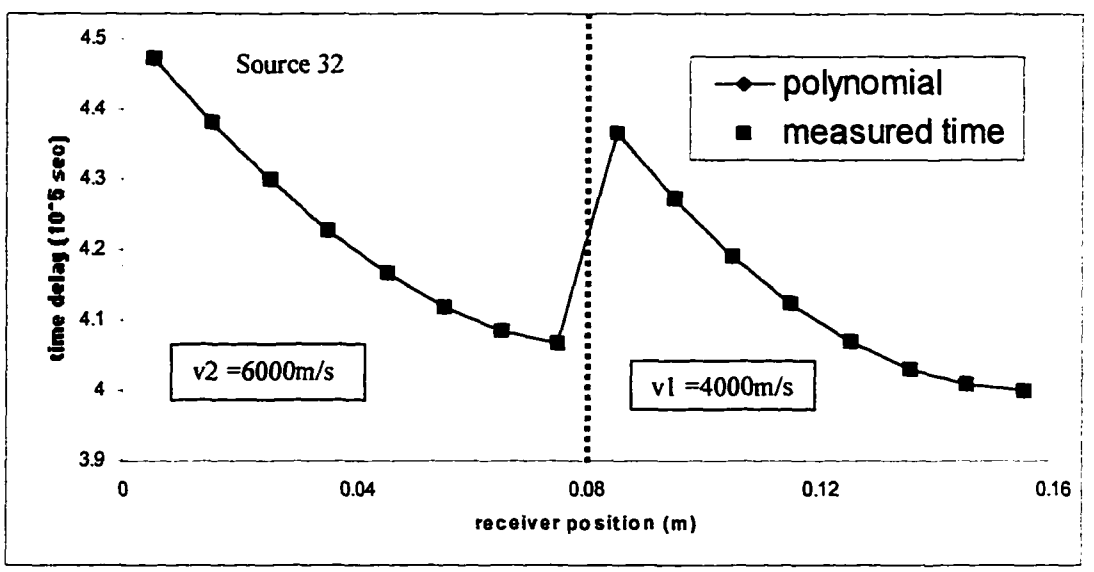


Figure 4.5 (b) Time delay curve for a single source. Both measured time and the polynomial approximation are shown.

A two-layer specimen is used in this example. The first layer has a velocity of 4000 m/s and the bottom layer has a velocity of 6000m/s. The time delay curve for a source on the upper right side with 16 receivers along the opposite side is shown in Figure 4.5 (b).

Receiver number one records the longest time delay curve, as the ray must cover the longest distance. The time delays decrease in a nonlinear fashion until the velocity boundary is crossed. At this point the time delay increases, since the ray is now propagating though a slower material. Two separate polynomial curves were used to approximate the time delay curve for source 32. If a launch angle is chosen so that a ray terminates at .032 cm from the bottom edge, a value for the "measured" time delay can be determined even though the termination point lies between the receiver positions at .025 cm and .035 cm.

While a significant timesaving has been achieved, the accuracy of the solution is now dependent upon the accuracy of the polynomial fit to the measured time delay curve. The effect of the polynomial curve fit will be discussed in the results section.

4.5 *Computational Examples and Results*

Some of the key concerns in developing an acoustic tomography algorithm are velocity boundary resolution and the speed of computation. Two models were tested in this study, a two-layer sample with a 50% velocity increase and an Epstein layer with a gradual 50% velocity increase, as shown in Figure 4.6.

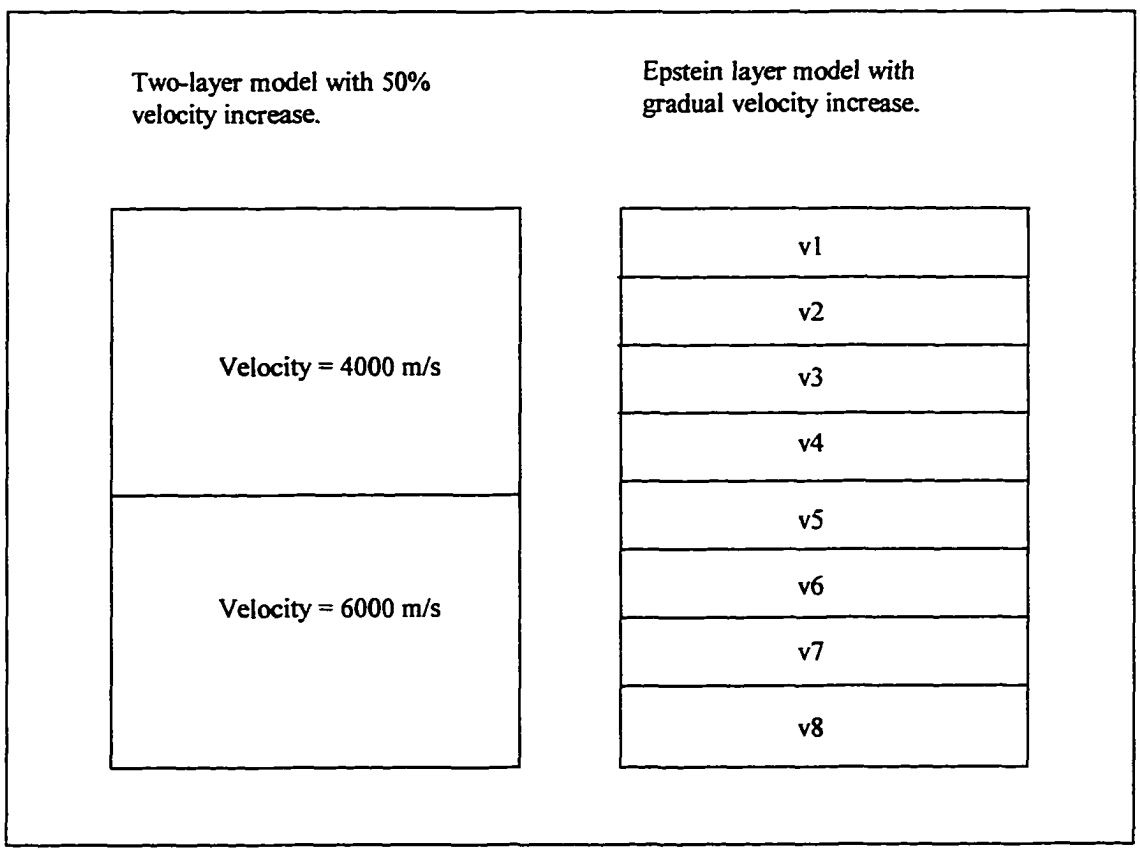


Figure 4.6 Models used in velocity reconstructions.

The source-receiver configurations were varied to test the velocity boundary resolution. Second and fourth degree polynomial approximations were used to approximate the time delay curve to determine the effect on the accuracy of the solution. The speeds of the parallel and the serial computations were compared as the array size increased.

The different source-receiver configurations tested are shown in Figure 4.7, and are outlined below:

A. sources along the top of the sample and receivers along the bottom.

B. sources along the top and receivers along the two sides and across the bottom.

C. sources along the top transmitting to receivers along the bottom and sources on the left side transmitting to receivers along the right side.

D. sources on the top and left side, all transmitting to receivers located along the other three sides.

The source receiver configurations had little effect on the accuracy of the Epstein layer samples. Good results were obtained with every configuration. An example of the reconstruction for an Epstein layer is shown in Figure 4.8.

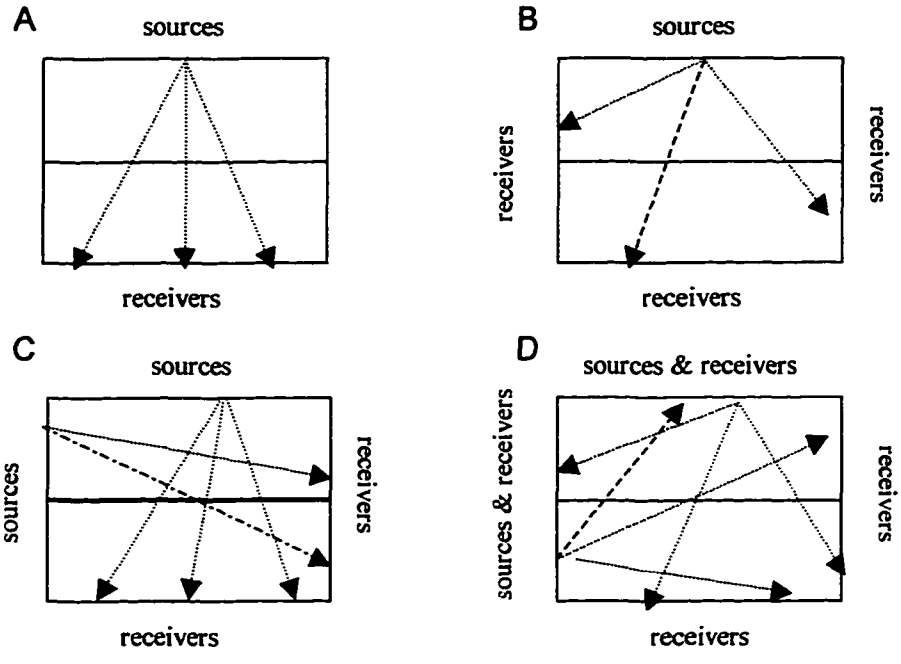


Figure 4.7 Source and receiver geometries.

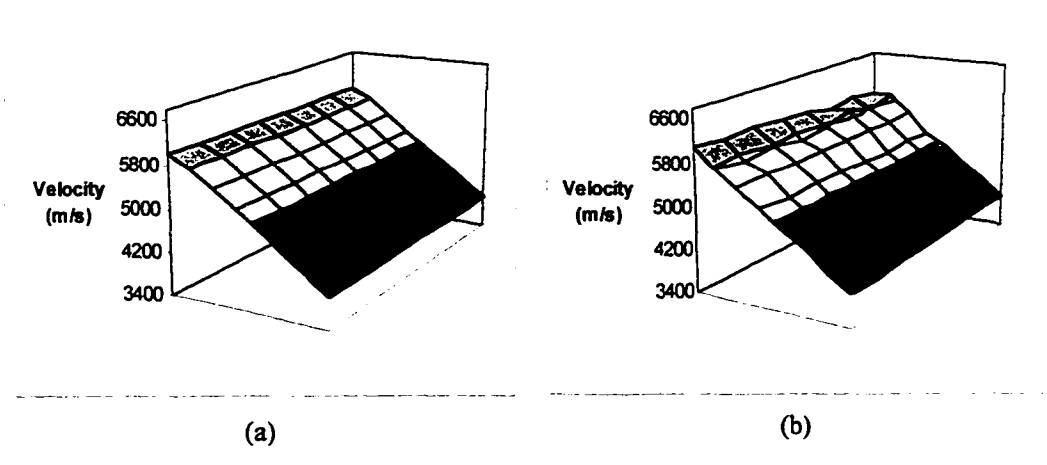


Figure 4.8 Epstein layer velocity reconstruction (a) simulated model and (b) reconstruction.

The solution to the two-layer problem was highly dependent on the source-receiver geometries. The solution for configuration A converged to a non-unique solution. For example, one solution may satisfy the time delay requirements for both a uniform 5000 m/s sample and a two-layer sample with velocities of 4000 m/s and 6000 m/s. Configuration B approached the correct solution but did not provide an accurate boundary between the two layers. The average error was 290 m/s or 7.25%. The average velocity error for each model was calculated by

$$v.e. = \frac{\sum \left| v_{ij}^{actual} - v_{ij}^{calc.} \right|}{number\ of\ spatial\ cells} \tag{4.13}$$

Significant improvement was achieved by using configuration C. The boundary between the two layers is clearly resolved and the velocity error is reduced to 20 m/s or 0.5%. Configuration D requires additional source-receiver pairs, but the accuracy of the solution has decreased. The boundary between the two layers is still clearly visible, but the velocity error has increased to 100 m/s. These results are shown in Figure 4.9 (a-d). As shown in Figure 4.10, the Epstein layer with the gradual 50% velocity increase converges more quickly then the two-layer model.

As the number of source-receiver pairs was increased, additional error was introduced into the system due to the uncertainty in the time delay approximation. This error is dependent on the degree of the polynomial approximation to the time delay curve. Originally a second-degree polynomial was used to approximate the time delay curve. The tomographic inversion was redone using a fourth-degree polynomial

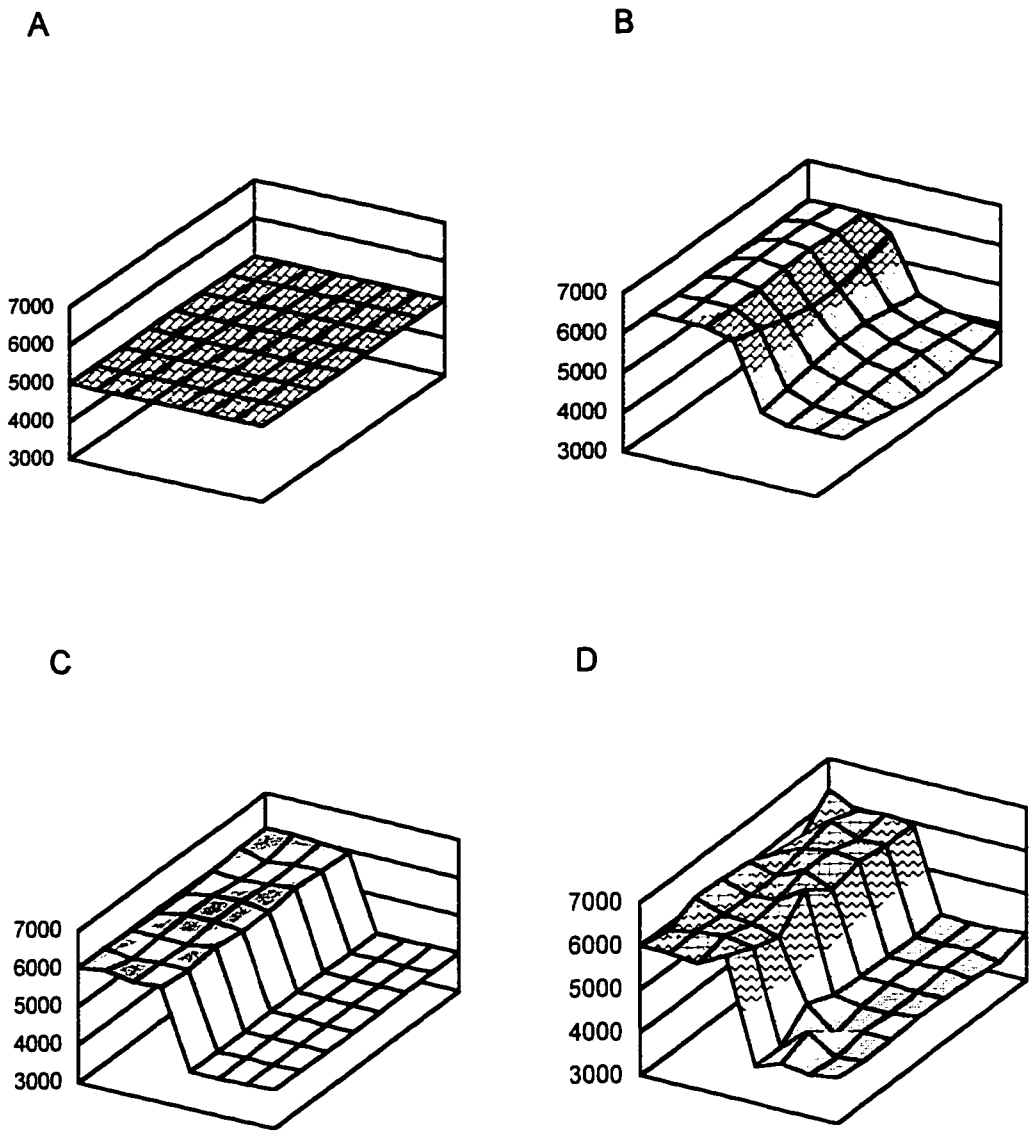


Figure 4.9 Tomographic reconstructions using the four different source-receiver combinations.

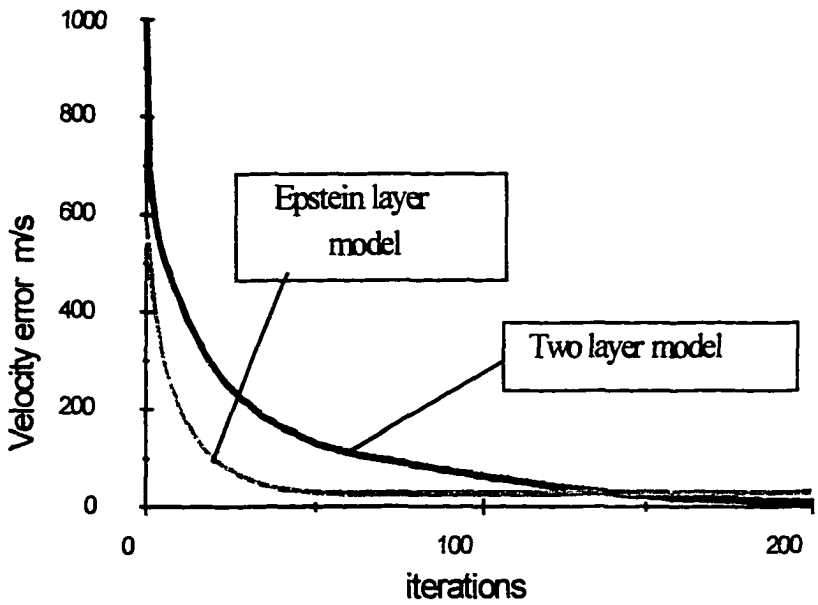


Figure 4.10 Comparison of convergence rates between the two-layer model and Epstein layer model.

approximation to the time delay curve. The error in the velocity calculations was significantly reduced. The convergence of the velocity error using a second-degree polynomial is shown in Figure 4.11 (a). The model is an 8 x 8 pixel grid with 512 source-receiver pairs, configuration (c). The error decreases rapidly during the first iterations and then converges to approximately 29 m/s after 200 iterations (error=0.6%). Figure 4.10(b) shows the difference between the second-degree and fourth-degree polynomial time delay approximations. After 200 iterations the velocity error using the fourth-degree polynomial approximation is only 9 m/s (error=0.2%).

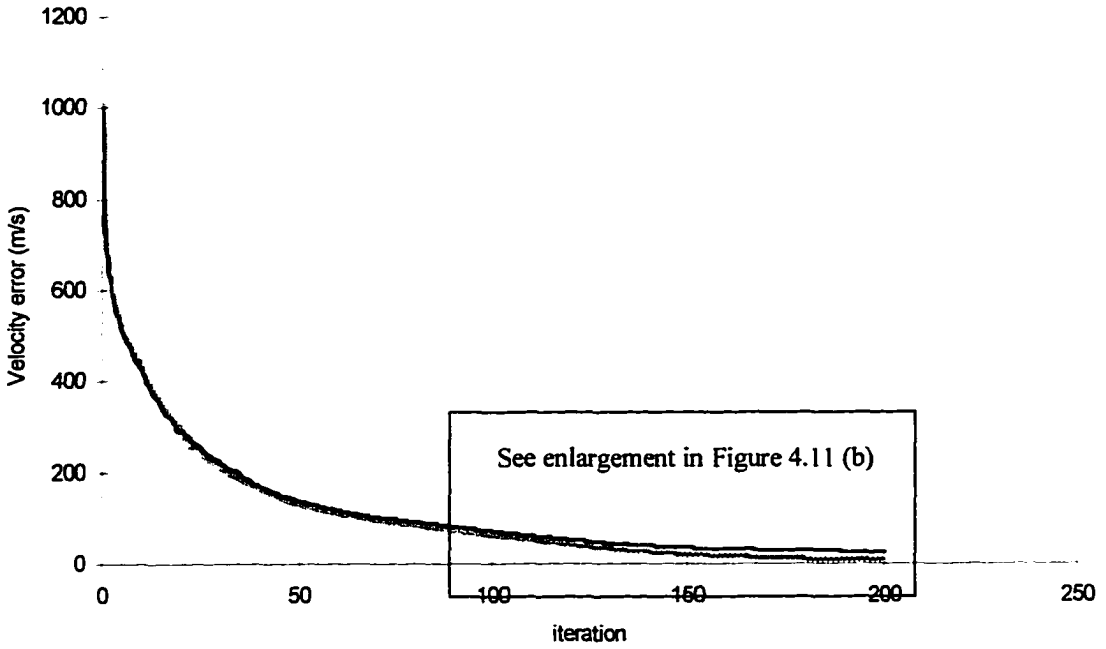


Figure 4.11 (a) Convergence of the velocity reconstruction using second-degree and fourth-degree polynomial approximations to the time delay curve.

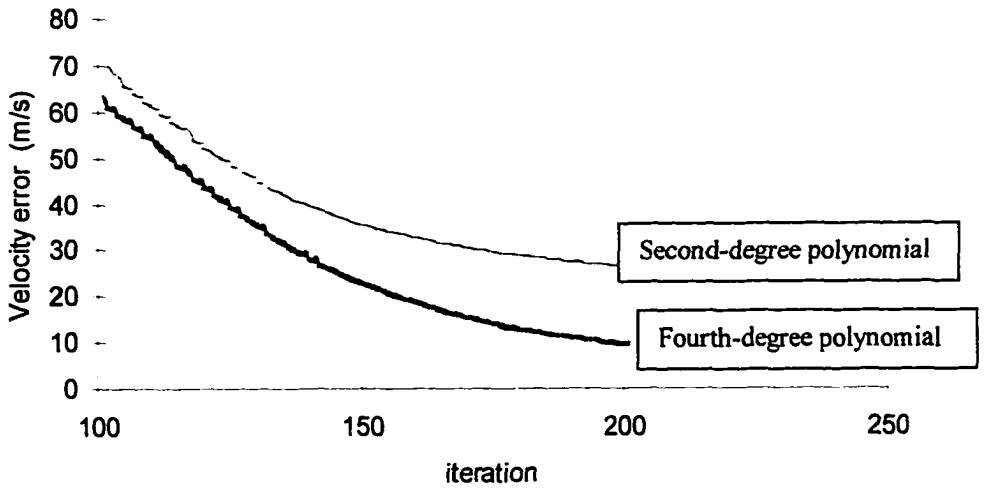


Figure 4.11 (b) Enlargement of Figure 4.11(a), iterations 100-200.

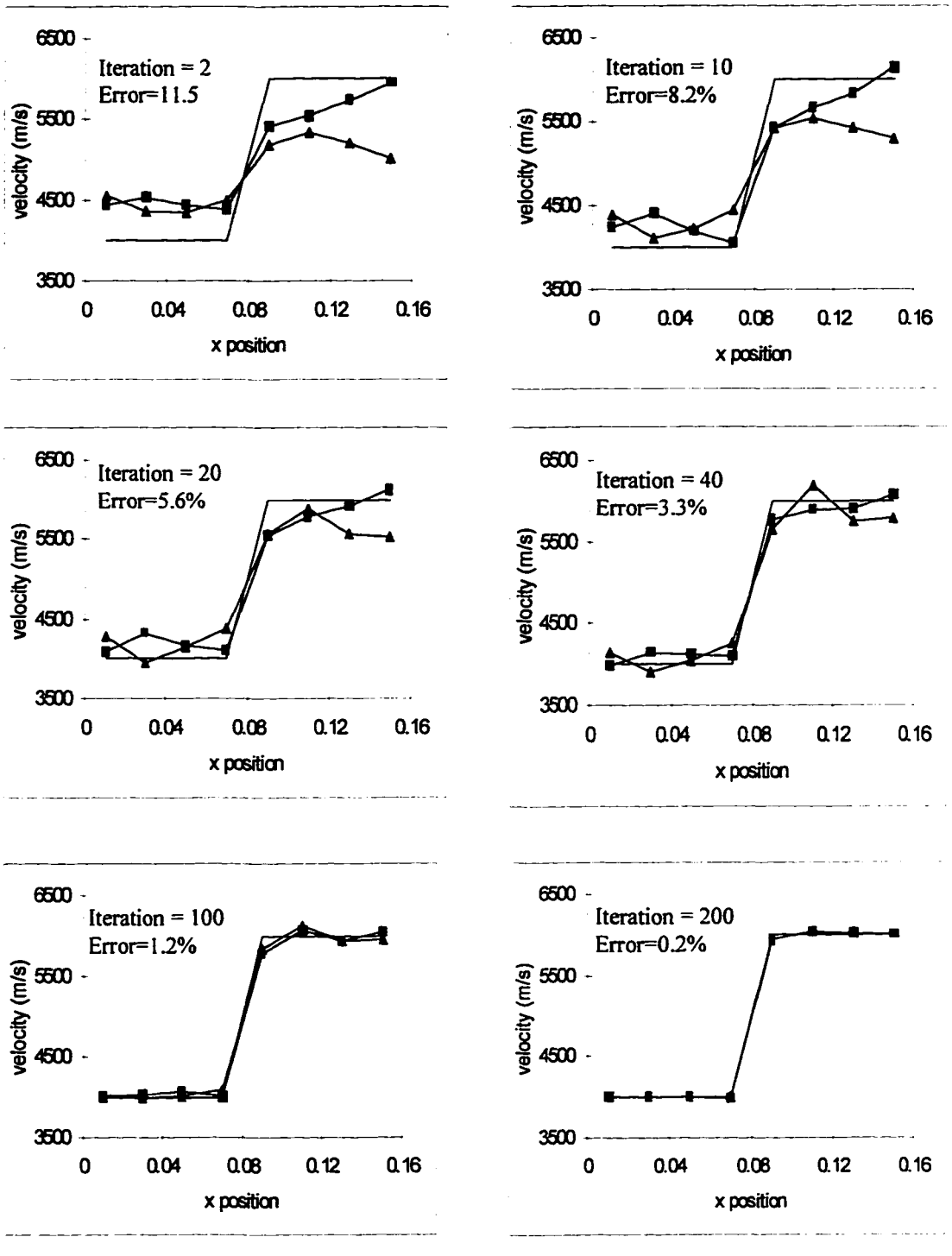


Figure 4.12 Cross-sectional "snapshots" of convergence process for the two-layer model, configuration (C).

Figure 4.12 shows cross-sectional "snapshots" of the convergence during the solution process. The solid line represents the actual velocity and the dotted lines represent the calculated velocities for the specified iteration. The solution is nearly complete after 100 iterations but requires 200 iterations for convergence to within 9m/s.

The tomographic inversion was performed for different array sizes, (array size equals the number of source-receiver pairs) ranging from 2^7 to 2^{13}, both in parallel and serial modes. The CPU time comparison is shown in figure 4.13. The SIRT algorithm is used for both the serial and parallel tomographic inversions. It can be seen that as the array size increases, the CPU time required for the serial solution

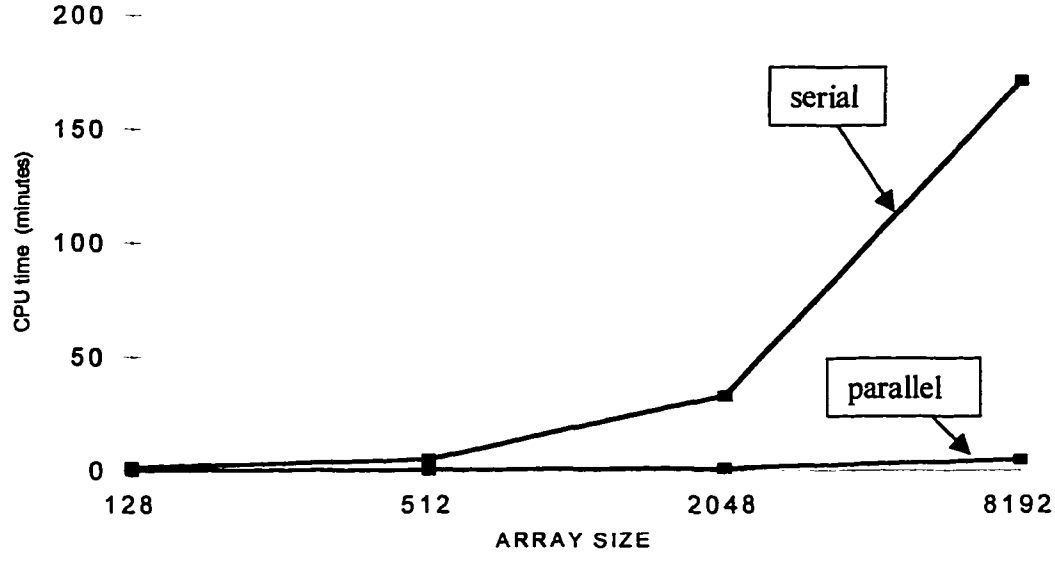


Figure 4.13 Comparison of CPU time for parallel and serial program.

increases dramatically. The CPU time required for the parallel solution remains relatively constant as the array size increases. This demonstrates the advantage of using parallel processing to handle large tomographic velocity reconstructions.

4.6 Anisotropic Materials

The models tested in the previous section were composed of isotropic heterogeneous materials. The ray-tracing algorithm assumed the energy propagated along the wave normal. In anisotropic media the energy propagates at the group velocity in the direction of the energy flux vector. This does not necessarily coincide with the wave normal. The acoustic velocity in each pixel is dependent upon the orientation of the ray path. The component of the group velocity, V_g, in the direction of the wave normal, l, is the phase velocity, V_p.

$$\vec{V}_g \bullet \hat{l} = \vec{V}_p \tag{4.14}$$

The phase velocity is related to the material properties as shown by the Christoffel equation, eq. (2.6). If the wave is propagating in the symmetry direction, the group velocity vector coincides with the wave normal.

An alternative formulation was used to perform tomographic reconstructions in anisotropic material. A full-field finite difference formulation was used to calculate the wave propagation through an orthotropic material. This method directly accounts for the anisotropy and the beam skewing effects. The method is presented in the next chapter.

CHAPTER IV

FULL-FIELD TOMOGRAPHIC RECONSTRUCTION

For the work discussed in the previous section, ray tracing was required to determine the path length of every ray across each pixel. These data were used to provide time delay information to the tomography algorithm.

$$t^{kl} = \sum_{i=1}^{n^2} a_i^{kl} s_i^m \tag{4.5}$$

Since the material was isotropic, each ray passing through the pixel measures precisely the same slowness as any other ray. If the material is anisotropic, the velocity measured in the pixel is dependent upon the orientation of the ray path. Kline and Wang[3] have accounted for this directional dependence by assuming weak anisotropy and straight ray paths.

Alternatively a full-field wave propagation approach can be used to determine the time delays through the material. The wave equation, equation (2.3), fully accounts for the anisotropy and directional dependence of the material. A finite difference formulation is used to calculate the displacements. The arrival of the quasi-longitudinal wave is recorded at specified receiver locations. The time delay for each source-receiver pair is sent to the tomographic algorithm and adjustments are made the stiffnesses (C_{ijkl}) of the material. Since the ray path distances are no longer

calculated a different formulation for the tomography algorithm is required. The algorithm used in this work is a based on the work of Kline and Wang[3]. They used a similar formulation to reconstruction Young's modulus of the epoxy matrix in a uniaxial fiber composite.

5.1 Tomography Algorithm

The wave equation and therefore the time delays of the source-receiver pairs are a function of the material stiffness.

$$T_{kl} = f_{kl}\left(C_{ij^1}, C_{ij^2}, \ldots C_{ij^n}\right) \tag{5.1}$$

The C_{ij} of a composite laminate are a function of many different parameters. In order to reconstruct the angle of rotation in each pixel, it is assumed that the only factor effecting the C_{ij} of the material is the alignment of the fibers.

$$C_{ij^1} = g_t(\theta_1, \phi_1) \tag{5.2}$$

For simplification, only the misalignment of the angle from the y axis in each pixel is considered.

$$C_{ij^1} = g_t(\theta_1) \tag{5.3}$$

Now the measured time delay of each source-receiver pair is a function of the fiber angle in each of the n pixels in the grid.

$$T^{kl} = f^{kl}\left(\theta_1, \theta_2, \theta_3, \ldots, \theta_n\right) = f^{kl}\left(\theta_i\right) \tag{5.4}$$

Likewise the calculated time delays from the m^{th} iteration are also a function of the angle.

$$t^{kl} = f^{kl}(\theta_i) \tag{5.5}$$

The current values of the rotation angle can be adjusted by an amount, $\Delta\theta$, so that the calculated time delays, t^{kl}, match the measured time delays, T^{kl}.

$$t^{kl} = f^{kl}(\theta_i + \Delta\theta_i) \tag{5.6}$$

Assuming adjustments to the current estimates of the angle are small, the above equation can be linearized by a Taylor Series.

$$t^{kl} = f(\theta_i) + \frac{\partial f^{kl}}{\partial \theta_i} + \text{H.O.T.} \tag{5.7}$$

Combining equations (5.7) and (5.4) to find the time delay difference results in

$$T^{kl} - t^{kl} = \Delta t^{kl} = \frac{\partial f^{kl}}{\partial \theta_i} \Delta\theta_i . \quad . \tag{5.8}$$

The method of Lagrange multipliers is used to impose the constraint that the magnitude of the changes in θ_i be minimized. In order to minimize the function

$$\Delta = \sum_{i=1}^{n^2} (\Delta\theta_i)^2 \tag{5.9}$$

a new function, L, is minimized

$$L = \sum_{i=1}^{n^2} \left((\Delta\theta_i)^2 - \lambda \frac{\partial f^{kl}}{\partial \Delta\theta_i} \Delta\theta_i \right) + \lambda \Delta t^{kl} \tag{5.10}$$

with respect to the change in angle.

$$\frac{\partial L}{\partial \theta_i} = 2\Delta\theta_i - \lambda \frac{\partial f^{kl}}{\partial \theta_i} = 0 \tag{5.11}$$

This requires

$$\Delta\theta_i = \frac{1}{2}\lambda \frac{\partial f^{kl}}{\partial \theta_i}. \tag{5.12}$$

Substituting the above equation into equation (5.8) and solving for λ gives

$$\lambda = \frac{2\Delta t^{kl}}{\sum_{kJ}\left(\frac{\partial f^{kl}}{\partial \theta_i}\right)^2} \tag{5.13}$$

Substituting the expression for λ into equation (5.12) results in the desired minimized correction factor for the angle of fiber rotation, θ.

$$\Delta\theta_i = \frac{\Delta t^{kl}\frac{\partial f^{kl}}{\partial \theta_i}}{\sum_{kJ}\left(\frac{\partial f^{kl}}{\partial \theta_i}\right)^2} \tag{5.14}$$

Similar to the tomographic reconstruction algorithm described previously, equation (4.10), a typical m^{th} iteration consists of

$$\theta_i^{m+1} = \theta_i^m + \lambda \Delta\theta_i^m \tag{5.15}$$

In the above equation, λ represents an artificial damping factor between 0 and 1.

The determination of the correction factor in equation (5.14) requires a calculation of the partial derivative, $\frac{\partial f^{kl}}{\partial \theta_i}$. This partial derivative can be computed by a first-order forward finite differences technique.

$$\frac{\partial f^{kl}}{\partial \theta_i} = \frac{t_{m+1}^{kl} - t_m^{kl}}{\Delta\theta} \tag{5.16}$$

The function, f^{kl}, is the time delay for the kl^{th} ray path. The derivative is calculated by perturbing the fiber angle a small amount, Δθ, in each pixel and recording the

change in the time delay in each ray path. The time delays are found from the finite difference solution to the wave equation.

5.2 *Finite Difference Solution of the Wave Equation*

There are two options to obtain a finite difference solution to the wave equation. One is to treat each cell as a discrete entity and balance the stresses and displacements at each interface.

$$\rho \ddot{u}_i = C_{ijkl} u_{k,lj} \tag{5.17}$$

The advantage to this method is that large acoustic impedance differences can be handled, but the boundary conditions are difficult. The method works very well for layered materials but has difficulty handling cross points were four different materials meet. and other edge type boundaries. Delsanto et al[18] have developed a program to handle an inhomogeneous orthotropic material with cross points. The program was written in parallel on the Connection Machine.

The second option has been used by Boore[40], Temple[41], and Harker and Oglivy[42]. The material is treated as a continuum and the material properties are allowed to vary with position along with the displacements.

$$\rho \ddot{u}_i = C_{ijkl} u_{k,lj} + u_{k,J} C_{ijkl,J} \tag{5.19}$$

Wang[39] used central finite differences to program equation (5.19) in parallel on the Connection Machine. The same formulation is used in this study. Each pixel is assigned a C_{ijkl}. The finite difference equation calculates the u_1 and u_2 components

(two-dimensional solution) of the displacements at the position (i,j) using the displacements from the nearest neighbors and the previous two time steps. The spatial calculations are done in parallel using a NEWS communication scheme. The time steps are done sequentially, as the wave progresses through the medium.

To ensure the stability of the solution, the size of the time step and the spatial step must be chosen with care. Alterman and Loewenthal[43] determined that the inequality

$$\frac{\Delta t}{h} \leq \sqrt{v_s^2 + v_l^2} \tag{5.20}$$

must be true to ensure stability for isotropic wave equations without boundary conditions. A trial-and-error approach to the selection of the time step and grid spacing is also acceptable. This study used a time step of 0.05 μs and a spacing step of 0.005m and the solution was stable.

The boundary conditions were specified to model a transducer coupling on one boundary and traction-free conditions on the receiver boundaries as was previously done by Wang[44]. Wang also studied the methods of detecting the arrival of the quasi-longitudinal wave. Three different parameters were studied (u - the displacement in the x direction, z - the modulus of the displacement, and e - the volumetric strain) along with three different arrival criteria (threshold, peak value and cross-correlation). The z modulus of the displacement

$$z = \sqrt{\left(u^2 + v^2\right)} \tag{5.21}$$

along with a peak value arrival criterion was found to be acceptable and was used in this study.

Before calculating the derivative $\frac{\partial f^{kl}}{\partial \theta_i}$, it must be determined whether the time delay curve is linear and also the appropriate step size for the finite difference formula, $\Delta\theta$, must be found. The effect of the angle of rotation on the time delay was studied by running the wave propagation algorithm while adjusting the angle of rotation for a single pixel by ½ degree increments from -20 to +20 degrees. Figure 5.1 shows the configuration of the source-receiver locations and the discretized grid. The time delay curves for source 1 and each of the receivers are shown in Figure 5.2. Pixel (4,4) has been rotated from -20 degrees to +20 degree in 1/2-degree increments.

The time delay from source 1 to the receivers on the left side, Figure 5.2 (a), is not affected by the change in angle of pixel (4,4). This is to be expected since these rays do not pass through this pixel. The effect of the fiber rotation in the single pixel can be seen in the time delays from source 1 to receivers on the lower right side, shown in Figure 5.2 (b). The relationship between the angle change and the time delay is clearly nonlinear. The receivers on the bottom side of the sample also show a slightly nonlinear effect as shown in Figure 5.2 (c) and (d). The nonlinear relation ship between the time delay and fiber angle indicates that $\Delta\theta$ should be small (one degree or less) or possibly a higher order approximation to the derivative should be used in the finite difference formula.

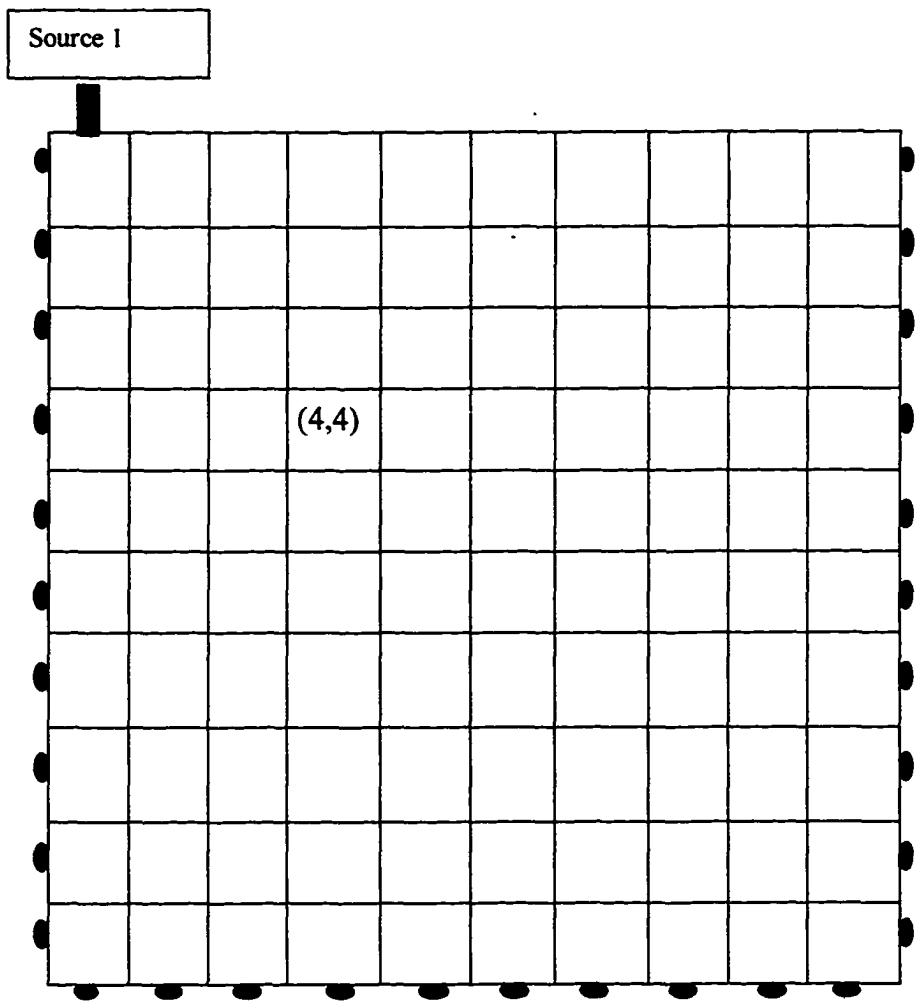


Figure 5.1 Source and receiver locations for time-delay computation on a 10X10 pixel grid. Sources are placed along the top of the sample. Only one source is shown.

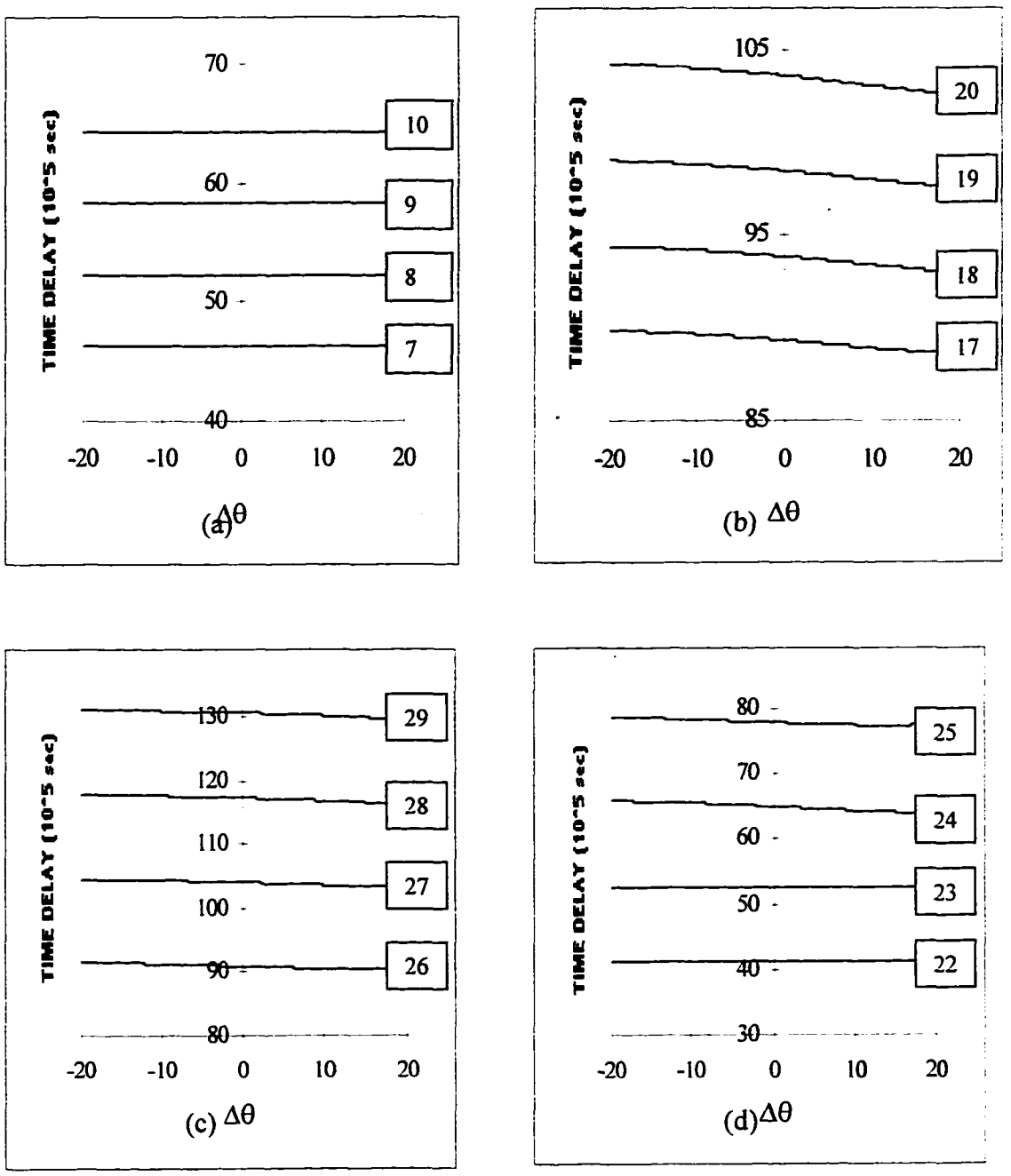


Figure 5.2 Effect of small angle change in pixel (4,4) on time delays. (a) source 1 to receivers on lower left side, (b) source (1) to receivers on lower right side, (c) source 1 to receivers on bottom left side, (d) source 1 to receivers on bottom right side.

Algorithm Design and Parallel Calculations

Unlike the ray-based tomographic reconstruction, not all source-receiver pairs are considered at one time. The wave propagation algorithm is simpler if it is run one source at a time. This eliminates interference from different wave fronts and any ambiguity about the first arrivals. One source at a time is "fired" but the time delays for all the receivers are calculated simultaneously. This allows the tomographic reconstruction algorithm described in section 5.1 to work on a source-by-source basis.

The first step in calculating the tomographic correction factor, equation (5.14), is to calculate the derivative. This is the most time-consuming procedure since a calculation must be made for each pixel, requiring a serial loop through the pixel grid. Each pixel is perturbed a $\Delta\theta$ and then the finite difference wave propagation is run for each source to determine $\frac{\partial f^{kl}}{\partial \theta_i}$. A 10 X 10 pixel grid with 10 sources requires 1000 iterations. It is desirable to configure the experimental set-up with a minimum number of sources and a maximum number of receivers since the receivers are calculated in parallel. Fortunately the derivative needs to be calculated only once and is not involved in the reconstruction iterations. The information from the derivative is stored in a four-dimensional array

$$tdtdr(k,l,i,j) = \frac{\frac{\partial f^{kl}}{\partial \theta_i}}{\sum_{k,l}\left(\frac{\partial f^{kl}}{\partial \theta_i}\right)^2}. \qquad (5.22)$$

Once the derivative information is found, the tomographic reconstruction begins and updates are made to each pixel angle. After the pixel angles have been changed the C_{ij} for each pixel are re-calculated before the wave propagation is run. The tomographic iterations consist of calculating the time delays, Δt^{kl}, and multiplying by equation (5.22).

The reconstructions were run for 200 iterations. The total CPU time for a 10 X 10 pixel grid is 52.3 minutes. The CPU time to calculate the derivative is 17.3 minutes or one third of the total time. The tomographic iterations take 35 minutes or 10.5 seconds per iteration.

The program is run for a specified number of iterations or until a convergence criterion is met. The following criterion was use in this study

$$R=\frac{1}{n^2}\sum_{i=1}^{n^2}\left|\theta_i^m-\theta_i^{m-1}\right| \tag{5.23}$$

The program is terminated when R is less then a specified number. A plot of R is shown in Figure 5.3. It can be seen the angle changes converge quickly; only very small changes are made after five or ten iterations.

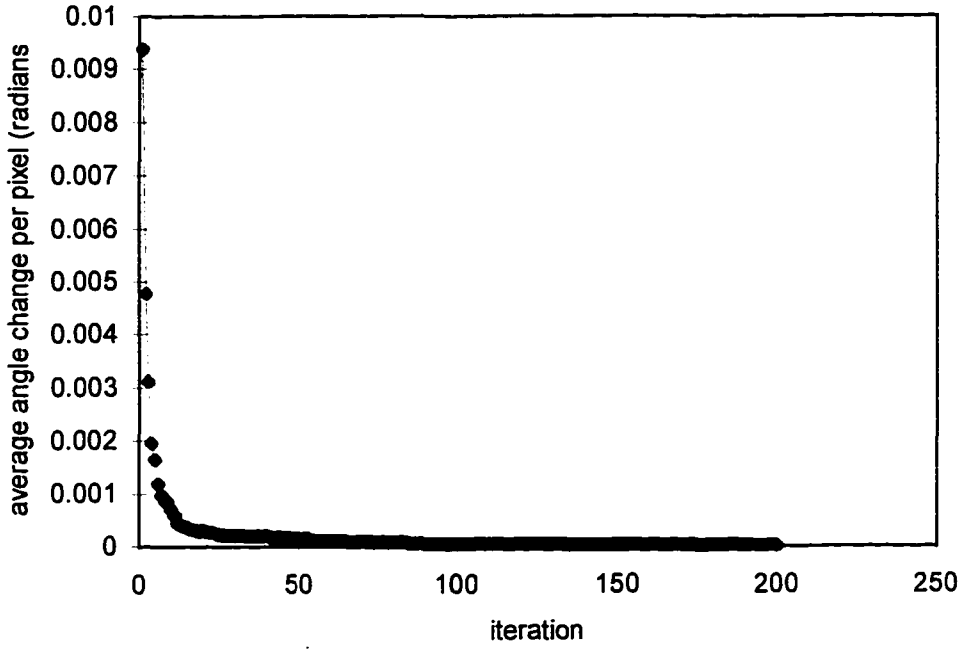


Figure 5.3 Convergence of tomographic reconstruction. The average angle change per pixel decreases rapidly.

5.4 *Reconstruction Results*

Good results were obtained using a first-order approximation to the derivative. Different rotations were applied to a small group of pixels, ranging from two to ten degrees. The quality of the results were dependent on the size of the perturbation, $\Delta\theta$, and the damping factor, λ.

Figure 5.4 shows the original set-up of 10 X 10 pixels with four pixels misaligned offcenter. The plan view is shown in Figure 5.4 (a) with a contour interval of 0.03 radians. The three-dimensional view is shown in Figure 5.4 (b). The accompanying reconstruction is shown in Figure 5.4 (c) and (d). The perturbation used was $\Delta\theta$=0.5 radians and the damping factor was set to 0.4. The sources are on the left side of the sample with receivers surrounding the other three sides. The reconstruction results are quite good. The pixels aligned at zero degrees fluctuate above and below the zero line from -.0.02 to +0.02 radians. (-1.0 to +1.0 degrees). There is a sharp distinction between the rotated and non-rotated pixels. The four rotated pixels converge to an average rotation of 1.71 radians or 9.8 degrees. A cross-section of the sample is shown in Figure 5.6, providing a "snapshot" of the convergence process. The location of the cross-section is shown in Figure 5.5.

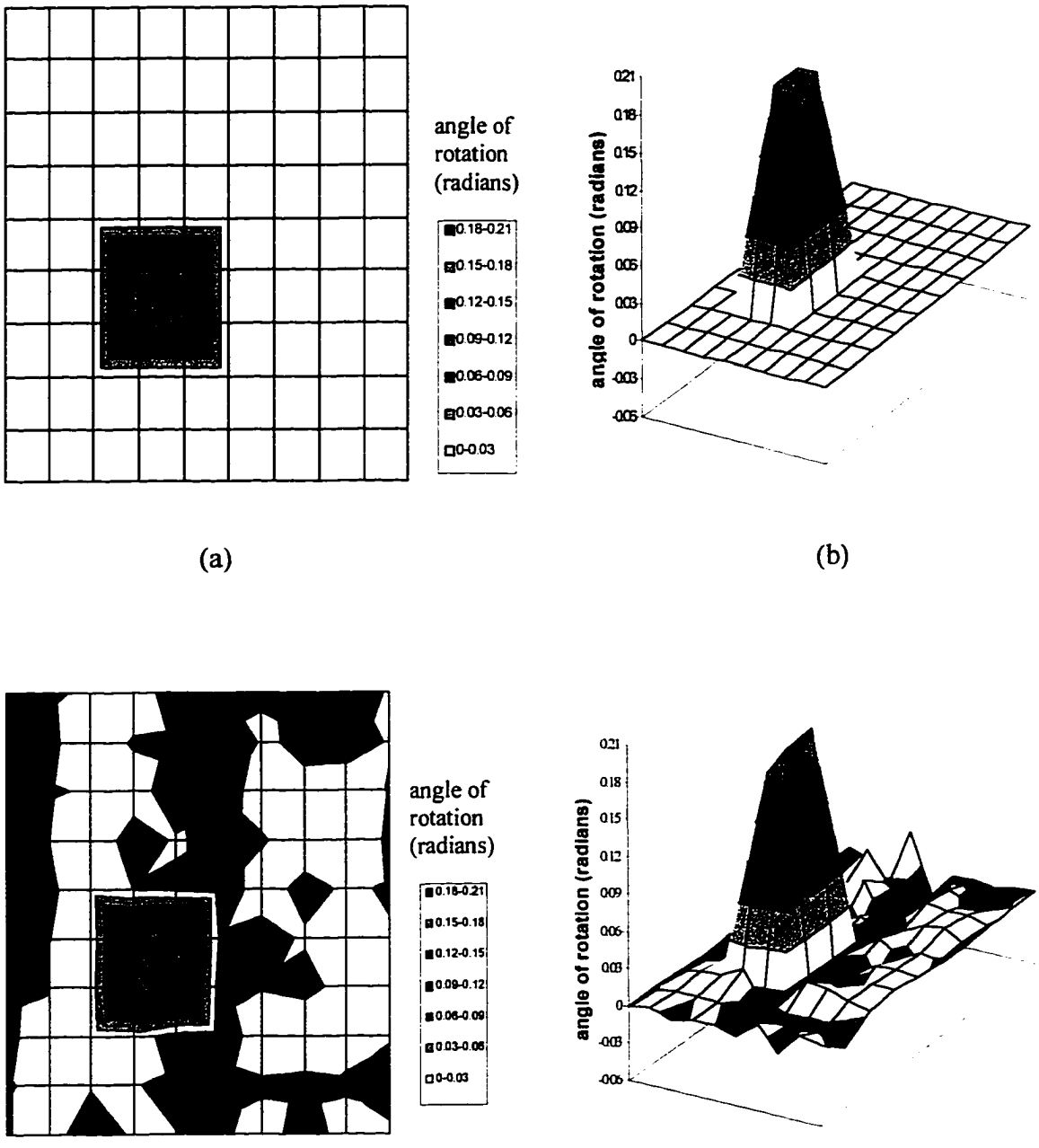


Figure 5.4 Tomographic reconstructions of a ten-degree rotation. The actual images are shown in (a) and (b) as a 2-D contour map and a 3-D representation respectively. The reconstructed images are shown in (c) and (d).

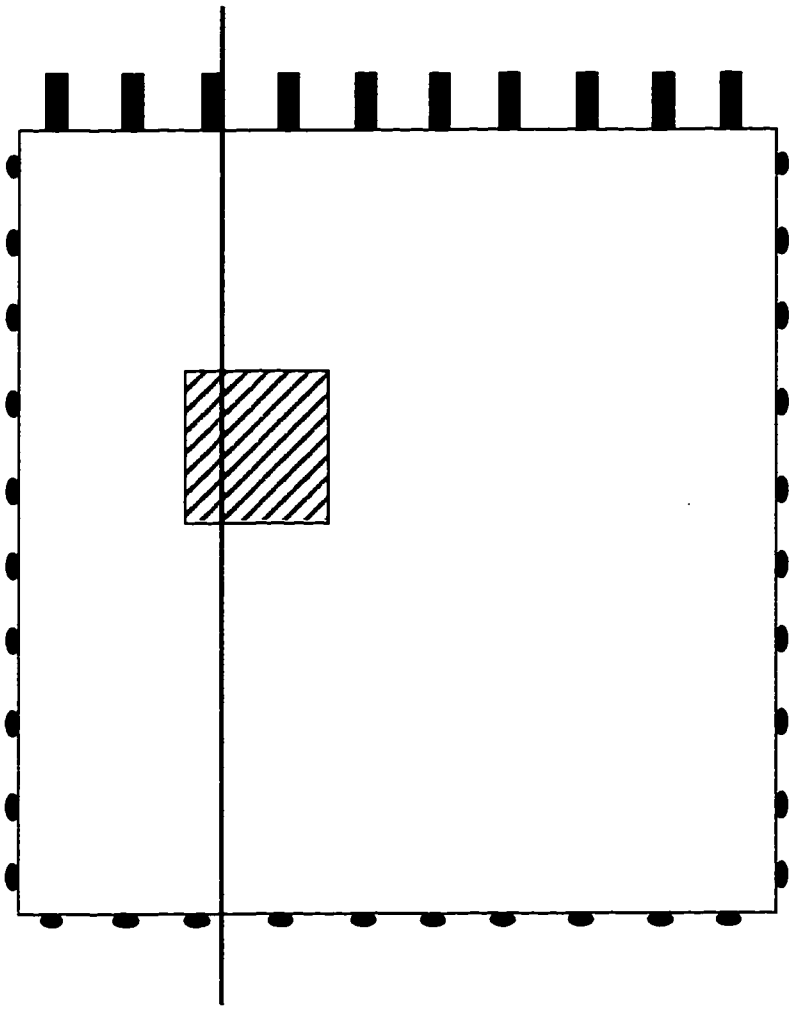


Figure 5.5 Location of cross-section of reconstructed image. Shaded area has been rotated ten degrees.

A three-degree rotation of the pixels can be detected., even after one rotation, as shown in Figure 5.6 The initial guess is a uniform, non-rotated (zero-degree) sample. By the fifth iteration the rotated pixels average eight degrees. Although not much change is made averaged over the entire grid after five iterations (see convergence plot, Figure 5.3), significant improvement is made in the isolation of the four rotated pixels. The non-rotated pixels get closer to zero and the rotated pixels approach an average of ten degrees.

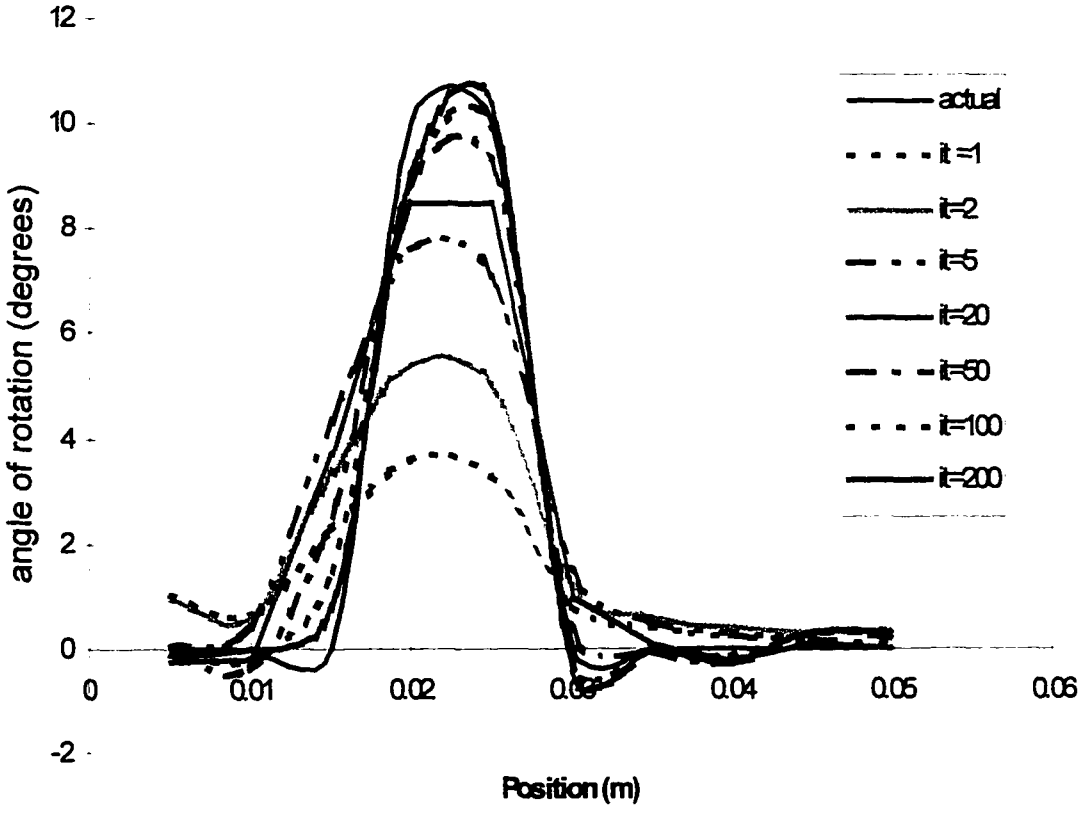


Figure 5.6 Snapshot of convergence process. Four pixels were rotated 10 degrees and progress of reconstruction is shown for different iterations.

There was concern that the algorithm may not be able to discern small misalignments due to the noise around the zero value in the previous reconstruction. The same configuration discussed above was run for a two degree misalignment in a single pixel. The results are shown in Figure 5.7. The perturbation used was $\Delta\theta$=0.25 radians and the damping factor was increased to 0.95. The reconstruction is more precise for a smaller angle of two degrees then a ten-degree rotation. This is because the formulation of the wave equation used in the wave propagation routine is best suited to small changes in the C_{ijkl}.

The effect of changing the perturbation, $\Delta\theta$, can be seen in Figure 5.8. The reconstruction results for a four pixel rotation of ten degrees are shown for three different values of $\Delta\theta$. Figure 5.8 (a) is the actual rotation. Figure 5.8 (b) is the reconstruction after 150 iterations and a $\Delta\theta$=3.0 degrees. In the upper section of the sample there are several areas where significant (-0.03 to -0.06 radians) negative rotations appear. The size of this area is reduced in Figure 5.8 (c) where a $\Delta\theta$=1.0 degree was used. The area of negative rotations has disappeared when a $\Delta\theta$=0.5 degrees is used as shown in Figure 5.8 (d). When a $\Delta\theta$=0.25 degrees is used the solution becomes unstable.

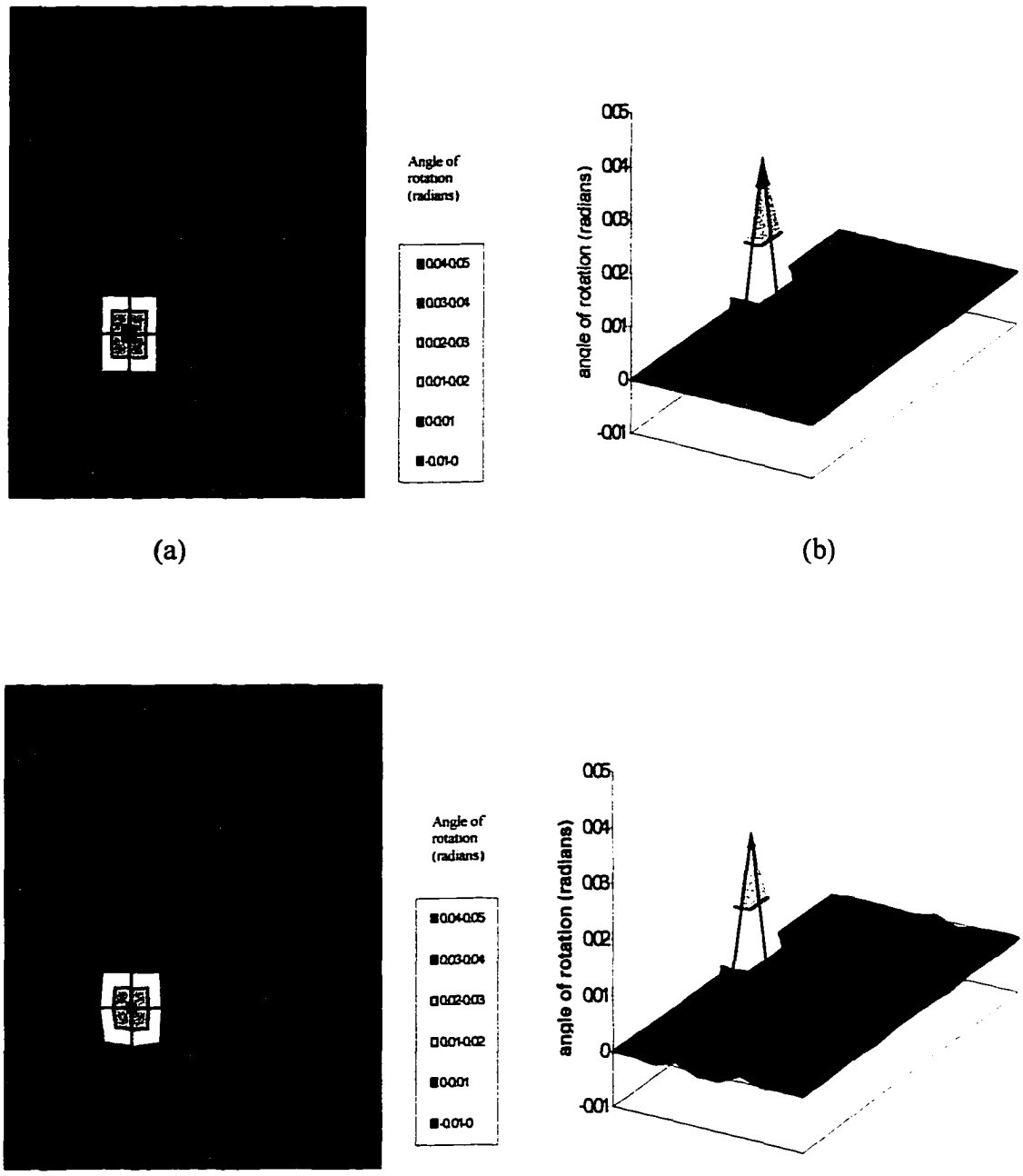


Figure 5.7 Tomographic reconstructions of a 2-degree rotation. The actual image is shown in (a) and (b) as a 2-D contour map and a 3-D representation respectively. The reconstructed image is shown in (c) and (d).

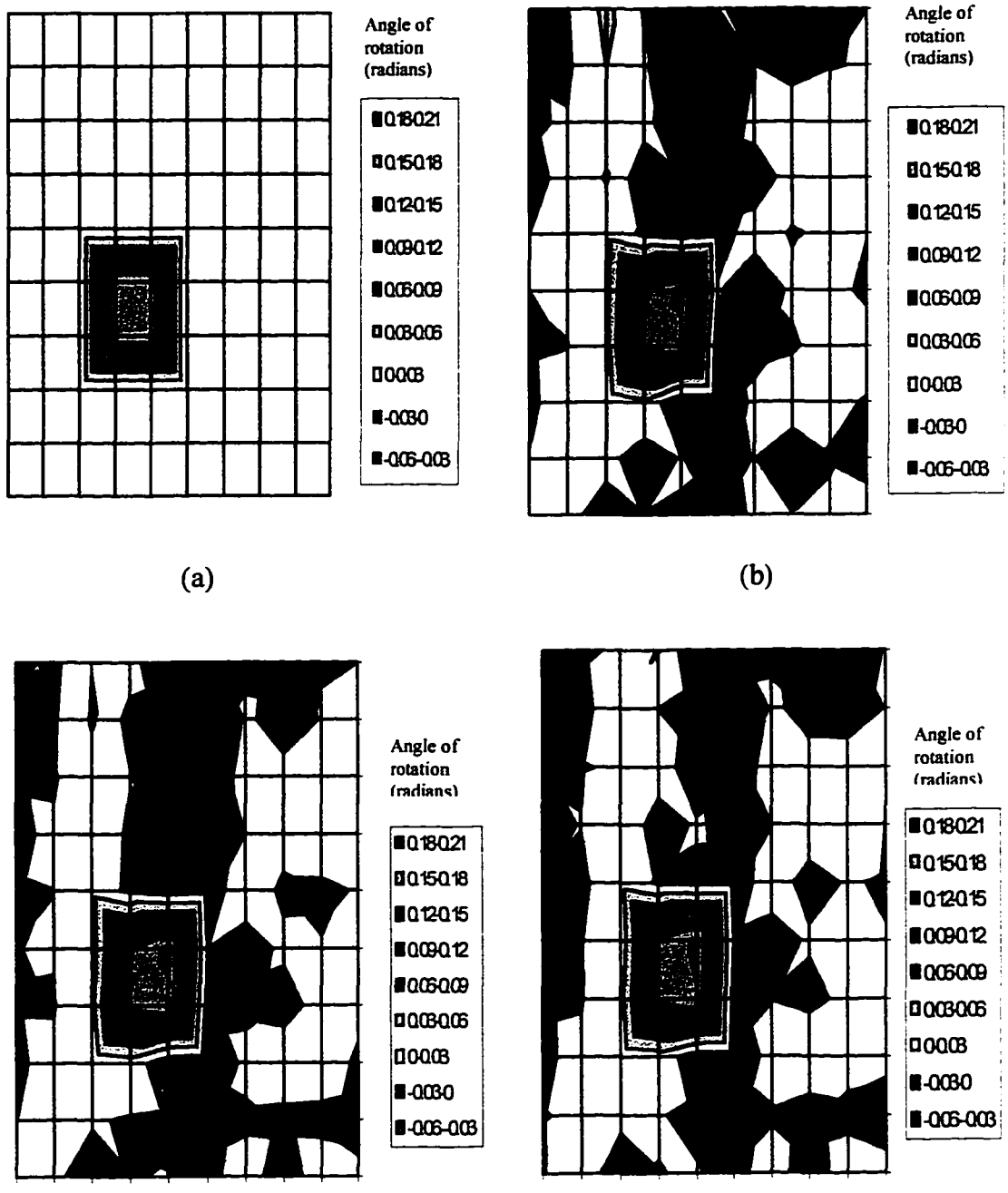
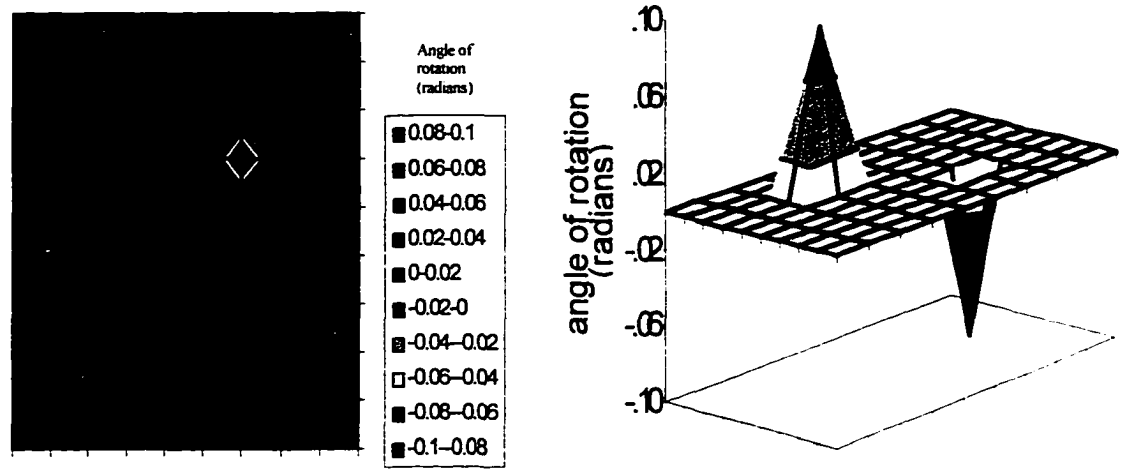


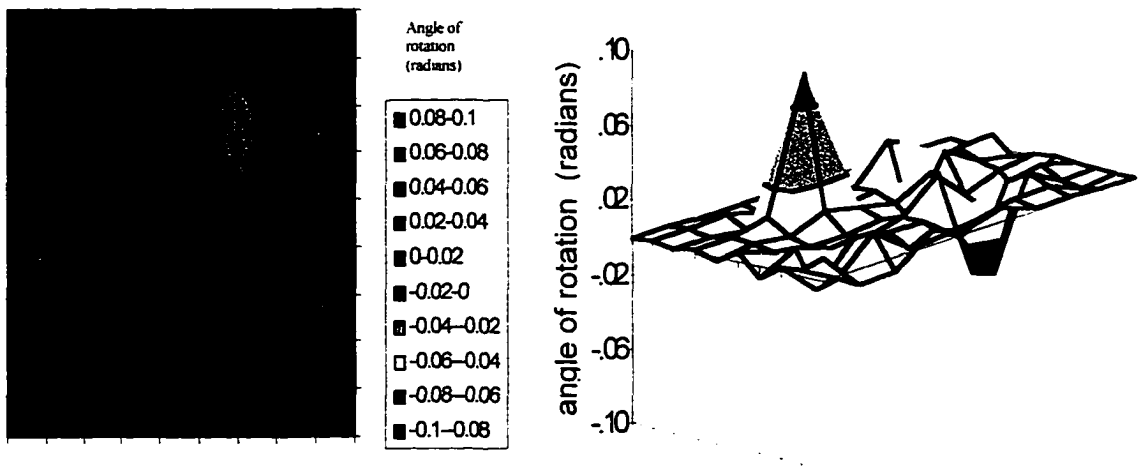
Figure 5.8 Effect of perturbation angle on reconstruction results.Figure 5.8 (a) is the model of the ten-degree rotation. The reconstruction using a $\Delta\theta$=3.0° is shown in (b), using a $\Delta\theta$=1.0° is shown in (c), and using a $\Delta\theta$=0.5° is shown in (d).

Since the tomographic algorithm looks at the time accumulated across the entire ray path and the rotation angle is updated using an average correction over all ray paths for each source, there was a concern that a symmetric +/- angle rotation might not be detected. The program was run for a 10 X10 pixel grid with two misaligned pixels. Pixel (4,4) was rotated a positive (CW) five degrees and pixel (7,7) was rotated a negative (CCW) five degrees. The results are shown in Figure 5.9 and 5.10. Figure 5.9 (a) and (b) shows the actual rotation in plan and three-dimensional view. The upper right anomaly is the negative rotation. Figures 5.9 (c) and (d) show the reconstruction results. The positive five-degree rotation is clearly seen, but the negative rotation is not as well defined. This sources are located on the left side, nearer the positive rotation. Figure 5.10 shows the three-dimensional reconstruction on a different scale. Although the negative rotation is not quantitatively accurate, its presence is easily detected.

The program was run using a second order approximation to the derivative in equation (5.14). This requires two perturbations of each pixel, $\Delta\theta$ and $2\Delta\theta$. Since this increases the CPU time significantly, the higher order derivative was tested on a 5 X 5 pixel grid. Figure 5.11(a) shows the reconstruction result of a five-degree rotation in a single pixel. A first order approximation to the derivative is used. Figure 5.11 (b) shows the same configuration with a second order approximation to the derivative. No significant improvement in the result was obtained.



(a) (b)



(c) (d)

Figure 5.9 Tomographic reconstructions of a positive five-degree and a negative five-degree rotation. The actual image is shown in (a) and (b) as a 2-D contour map and a 3-D representation respectively. The reconstructed image is shown in (c) and (d).

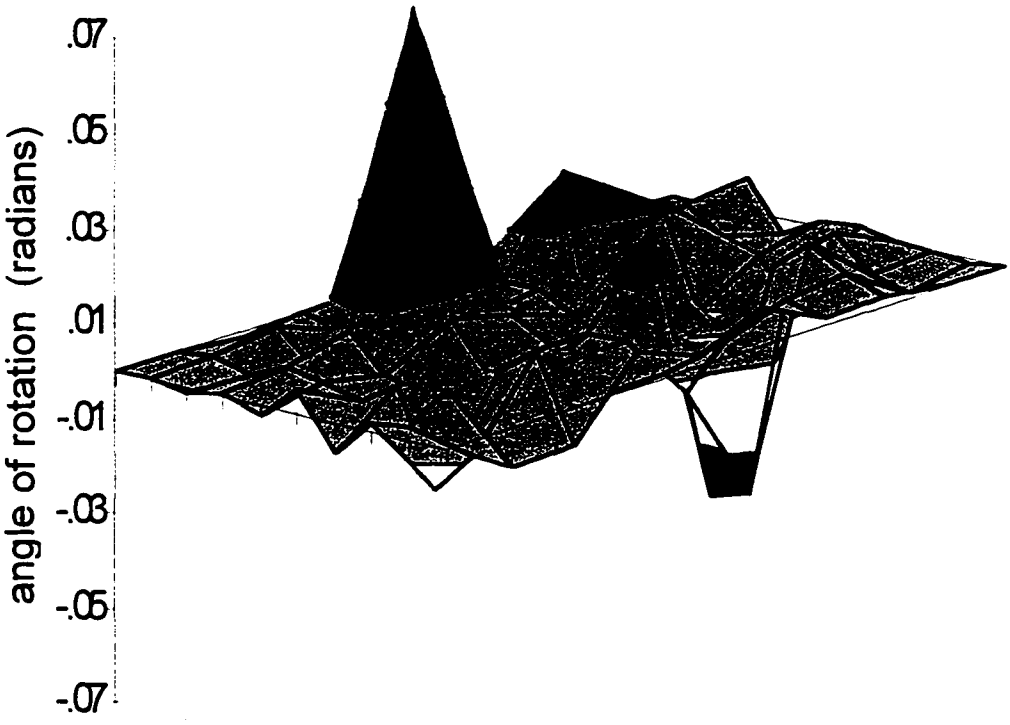
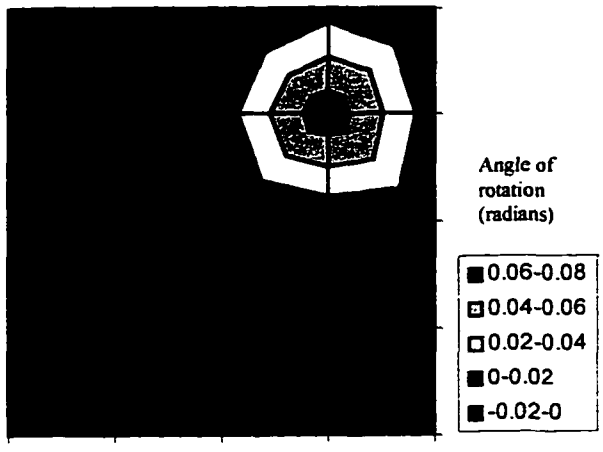
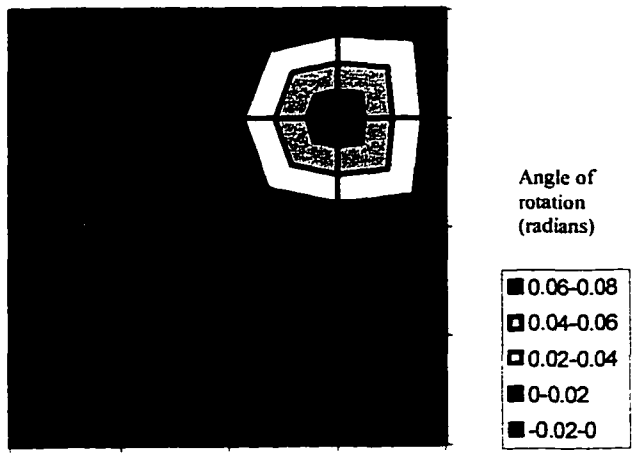


Figure 5.10 Tomographic reconstruction of a positive five-degree and a negative five-degree rotation.



(a)



(b)

Figure 5.11 Reconstruction of a five-degree rotation using a 5 X 5 pixel grid. (a) first-order approximation to the derivative is used and (b) second-order approximation to the derivative is used.

CHAPTER VI

CONCLUSIONS

A parallel approach to acoustic tomography has been developed. A ray tracing technique was applied to a nonhomogeneous isotropic sample and a finite difference approach was used for anisotropic media.

The ray tracing procedure is based on Snell's Law. The use of a polynomial approximation to the time delay curve eliminated the need to apply a shooting method to determine boundary conditions. The tomographic inversion used is a parallel version of SIRT. The reconstruction parameter was the velocity.

Different source-receiver configurations and different sized arrays of sources and receivers were tested to determine the accuracy and the speed of the parallel tomographic inversion. Sources along the side of the model were required to accurately resolve the velocity boundary in the two-layer model. Results from the Epstein layer model were independent of the source-receiver configuration; good results were achieved for each configuration. Increasing the degree of the polynomial curve for the time delay data reduced the average velocity error. Convergence rates for the Epstein layer and the two-layer model were compared. It was found that the

gradual velocity changes in the Epstein layer converged to a solution quicker then the abrupt 50% change in velocity in the two-layer model.

The CPU time required for the solution of the tomographic inversion was compared for serial and parallel operations. The time required for small problems was compared for the parallel and serial programs. The CPU time required for the solution of the serial operation increased dramatically as the array size increased, limiting the applicability of the technique. The CPU time required for the parallel solution remained relatively constant as the problem size increased, demonstrating the suitability of the technique for complex problems.

A program was developed to handle a full-field wave-propagation-based tomography algorithm on a parallel computer. The solution to the wave equation was calculated using a finite difference method exploiting the NEWS communication scheme of the Connection Machine. The algebraic reconstruction technique was modified to reconstruct fiber angles in an orthotropic composite laminate. This was accomplished by weighting the angle correction by a sensitivity factor based on the effect of the angle change on the travel time through the specimen.

The effect of a fiber angle rotation on the time delay was found to be slightly nonlinear. However, it was determined that a second-order approximation to the derivative was not necessary. The step size used to calculate the first order derivative did have an effect on the results. It is important that the perturbation of the rotation angle used in the derivative calculation be sufficiently small.

The full-field wave propagation approach proved extremely adept at reconstructing material properties in anisotropic materials. Changes in fiber angle from two to ten degrees were easily detected. Not only was the presence of the misalignment detected, but the quantitative amount of the rotation was also determined.

REFERENCES

1 R.K. Muellwe, M. Kaveh, and G.Wade, " Reconstructive Tomography and Applications to Ultrasonics", Proceedings of the IEEE, Vol. 67(4), 567-587 (1979)

2 G. Wade, "Ultrasonic Imaging by Reconstructive Tomography", Acoustical Imaging, Vol. 9, 379-431

3 R.A. Kline and Y.Q. Wang, " A Technique for Ultrasonic Tomography in Anisotropic Media", J. Acoust. Soc. Am. , Vol. 91(2), 878-884 (1992)

4 C.M. Sehgal and J.F. Greenleaf, "Ultrasonic Computed Tomography for Imaging Bones and Adjoining Soft Tissues", Materials Research Society Symposium Proceedings, Vol. 217, 157-156

5 D.W. Ratcliff, "Mahogany Salt Images Show Key Role of Velocity Model", Oil and Gas Journal, 43-53 (24-Oct. 1994)

6 W.S. French, "Improvements in 3-D Seismic", World Oil, Vol. 215, 60-61 (1994)

7 R.J. Lytle and K.A. Dines, "Iterative Ray Tracing Between Boreholes for Underground Image Reconstruction, " IEEE Trans. Geosci. Remote Sensing, Vol. 18 (3), 234-240 (1980)

8 J. Um and C. Thurber, "A Fast Algorithm for Two-Point Seismic Ray Tracing", Bull. Sesismol. Soc. Am. Vol. 77(3), 972-986 (1987)

9 E. Asakawa and T. Kawanaka, "Seismic Ray Tracing using Linear Traveltime Interpolation", Geophys. Preospect., Vol. 41, 99-111 (1993)

10 T. Zhu and K. Chun, "Complex Rays in Elastic and Anealastic Media", Geophys. J. Int., Vol. 119, 269-276 (1994)

11 R. Fischer and J.M. Lees, " Shortest Path Raytracing with Sparse Graphs", Geophysics, Vol. 58 (7), 987-996 (1993)

12 T. Moser, "Shortest Path Calculation of Seismic Rays", Geophysics, Vol. 56 (7), 59-67 (1991)

13 R. Snieder and M. Sambridge, "Ray Perturbation Theory for Traveltimes and Ray Paths in 3-d Heterogeneous Media", Geophys. J. Int., Vol. 109, 294-321 (1992)

14 V. Farra, "Ray Tracing in Complex Media", Journal of Applied Geophysics Vol. 30, 55-73 (1993)

15 Y.Q. Wang and R. A. Kline, " Ray Tracing in Isotropic and Anisotropic Materials: Application to Tomographic Image Reconstruction", J. Acoust. Soc. Am., Vol. 95 (5), 2525-2532 (1994)

16 J.R. Matarese, "Nonlinear Traveltime Tomography," Ph.D. dissertation, MIT, 1993

17 C. Sullivan, Kline, R.A., R.B. Mignogna, and P.P. Delsanto, "A Parallel Processing Approach to Acoustic Tomography", J. Acoust. Soc. Am. Vol. 99(4), 2142-2147 (1996)

18 P.P. Delsanto,T.Whitcombe, H.H. Chaskelis and R.B. Mignogna, "Use of the Connection Machine to Study Ultrasonic Wave Propagation in Materials",

Review of Progress in Quantitative Nondestructive Evaluation, Vol. 9, 141-148, (1990)

19 P.P. Delsanto, R. Schechter, H.H. Chaskelils, R.B. Mignogna, "Connection Machine Simulation of Ultrasonic Wave Propagation in Materials, II: The Two-Deimesional Case," Wave Motion , Vol 20, 295-314 (1994)

20 R.S. Schechter, H.H. Chaskelis, R.B. Mignogna, and P.P. Delsanto, " Real-time Parallel Computation and Visualization of Ultrasonic Pulses in Solids" Science Vol. 265 (5176), 1188-1196 (1994)

21 D.W. Vasco and E.L. Majer, "Wavepath Traveltime Tomography", Geophys. J. Int., Vol. 115, 1055-1069 (1993)

22 P. Podvin and I. Lecomte, " Finite Difference Computation of Traveltimes in Very Contrasted Velocity Models: A Massively Parallel Approach and its Associated Tools", Geophys. J. Int., Vol. 105, 271-284 (1991)

23 R.A. Kline, Y.Q. Wang, R.B. Mignogna, and P.P. Delsatnto, "A Finite Difference Approach to Acoustic tomography in Anisotropic Media", Journal of Nondestructive Evaluation, Vol. 13 (2), 75-83 (1994)

24 C.J. Ammom and J.E. Vidale, "Tomography Without Rays", Bull. Seism. Soc. Am., Vol. 83 (2), 509-528 (1993)

25 G.T. Schuster and A. Quintus-Bosz, " Wavepath Eikonal Traveltime Inversion: Theory", Geophysics, Vol. 58 (9), 1314-1323 (1993)

26 S.C. Wooh and I.M. Daniel, "Wave Propagation in Composite Materials with Fibre Waviness", Ultrasonics, Vol. 33(1), 3-10 (1995)

27 R.C. Reuter, Jr., "Concise Property Transformation Relations for an Anisotropic Lamina, J. Composite Materials, 112-114, (1971)

28 R. M. Jones, *Mechanics of Composite Materials*, Hemisphere Publishing Corporation, New York, (1975)

29 Z. Hashin and B.W. Rosen, "The Elastic Moduli of Fiber-Reinforced Materials", J. Applied Mechanics, Vol. 31, 223-232 (1964)

30 J.C. Halpin and S.W. Tsai, :Effects of Environmental Factors on Composite Materials, AFML-TR, 67-423 (1969)

31 G. Astfalk, "Fundamentals and practicalities of MPP", The Leading Edge, 839-843 (August, 1993)

32 L.W. Tucker, and G.C. Robertson, "Architecture and Applications of the Connection Machine", Computer Proceedings of the IEEE, 27-38(August, 1988)

33 W. Daniel Hills, The Connection Machine, MIT Press, Cambridge, MA (1985)

34 Thinking Machines Corporation, "The CM Fortran Programming Guide" Version 1.0 (1991)

35 R.T. Langan, I.Lerche, and R.T. Cutler, "Tracing of Rays through a Heterogeneous Media: An Accurate and efficient procedure", Geophysics, Vol. 50(9), 1456-1465 (1985)

36 R.R. Stewart, Exploration Seismic Tomography: Fundamentals, Course Notes, Vol. 3, Society of Exploration Geophysicists, (1991)

37 A. van der Sluis and H.A. van der Vorst, "Numerical Solution of Large Sparse Linear Algebraic Systems Arising from Tomographic Problems," in *Seismic*

Tomography: With Applications in Global Seismology and Exploration Geophysics, G. Nolet ed, D. Reidel Publishing, Holland, 49-85 (1987).

38 W.M. Telford, L.P. Geldart, R.E. Sheriff, and D.A. Keyes, Applied Geophysics, Cambridge University Press (1976)

39 S.C. Chapra, and R.P.Canale, Numerical Methods for Engineers, McGraw-Hill, New York, (1988)

40 R. Boore, in *Methods in Computational Physics,* Vol. 11, B.A. Bolt, ed. (Academic Press, New York, 1992)

41 J. Temple, "Modeling the propagation media", *J Phys. D: Applied Phys.* Vol. 21, 849-874 (1988)

42 A.H. Harker and J.A. Ogilivy, "Coherent Wave Propagation in Inhomogeneous Materials: A Comparison of Theoretical Models, *Ultrasonics*, Vol. 29(5), 235-244 (1991).

43 Z. Alterman and D. Loewenthal, "Seismic Waves in a Quarter Plane and Three-Quarter Plane", *Geophysical Journal of the Royal Ast. Soc.*, Vol. 20, 101-126 (1970).

44 Y. Wang, "Ultrasonic Tomography in Fiber Reinforced Composite Materials", Ph.D. dissertation, University of Oklahoma, (1993).